

In Situ Ligand Formation in the Synthetic Processes from Mononuclear Dy(III) Compounds to Binuclear Dy(III) Compounds: Synthesis, Structure, Magnetic Behavior, and Theoretical Analysis

Sheng Zhang,* Jiamin Tang, Jin Zhang, Fang Xu, Sanping Chen,* Dengwei Hu, Bing Yin,* and Jiangwei Zhang*

Cite This: *Inorg. Chem.* 2021, 60, 816–830

Read Online

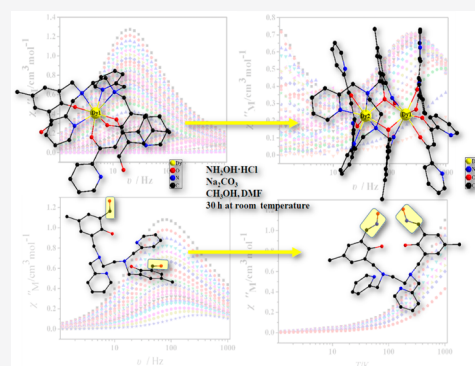
ACCESS |

Metrics & More

Article Recommendations

Supporting Information

ABSTRACT: Guided by the self-assembled process and mechanism, the strategy of in situ Schiff base reaction would be capable of bringing a feasible method to construct and synthesize lanthanide compounds with distinct structures and magnetic properties. A mononuclear Dy(III) compound was synthesized through a multidentate Schiff base ligand and a chelating β -diketonate ligand, which was named as $[\text{Dy}(\text{L})(\text{bppd})] \cdot \text{CH}_3\text{OH}$ [1; $\text{H}_2\text{L} = \text{N},\text{N}'$ -bis(2-hydroxy-5-methyl-3-formylbenzyl)- N,N' -bis(pyridin-2-ylmethyl)ethylenediamine and $\text{bppd} = 3$ -bis(pyridin-2-yl)propane-1,3-dione]. Furthermore, a new binuclear Dy(III) compound, $[\text{Dy}_2(\text{H}_2\text{Lox})(\text{bppd})_3] \cdot 8\text{CH}_3\text{OH}$ [2; $\text{H}_4\text{Lox} = \text{N},\text{N}'$ -bis[2-hydroxy-5-methyl-3-(hydroxyiminomethyl)benzyl]- N,N' -bis(pyridin-2-ylmethyl)ethylenediamine], was obtained via an in situ synthetic process. Under similar synthetic conditions, $[\text{Dy}(\text{L})(\text{ctbd})]$ [3; $\text{ctbd} = 1$ -(4-chlorophenyl)-4,4,4-trifluoro-1,3-butanedione] and $[\text{Dy}_2(\text{H}_2\text{Lox})(\text{ctbd})_3] \cdot \text{CH}_3\text{OH} \cdot \text{C}_4\text{H}_{10}\text{O}$ (4) were synthesized by modifying the β -diketonate ligand and in situ Schiff base reaction. Compound 3 is a mononuclear configuration, while compound 4 exhibits a binuclear Dy(III) unit. Therein, formylbenzyl groups of H_2L in 1 and 3 were changed to (hydroxyiminomethyl)benzyl groups in 2 and 4, respectively. In isomorphous 2 and 4, two Dy(III) centers are connected through two phenol O^- atoms of the $\text{H}_2\text{Lox}^{2-}$ ligand to form a binuclear structure. Eight-coordinated Dy(III) ions with different distortions can be observed in 1–4. The crystals of 1 and 3 suffered dissolution/precipitation to obtain 2 and 4, respectively. The relationship between the structure and magnetism in compounds 1–4 was discussed through the combination of structural, experimental, and theoretical investigations. Especially, the rates of quantum tunneling of magnetization of 1–4 were theoretically predicted and are consistent with the experimental results. For 2 and 4, the theoretically calculated dipolar parameters J_{dip} are consistent with the experimental observation of weak ferromagnetic coupling.



INTRODUCTION

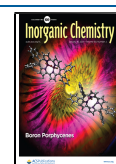
Researchers in all fields of science constantly seek strategies for controllable synthesis in order to control as many experimental variables as possible. This provides a rational synthesis process and governs the outcome of the experiment. The final objective is to realize target products and understand the dominant parameters of the overall behavior. Controllable syntheses of coordination polymers possessing single-ion magnets (SIMs) or single-molecule magnets (SMMs) are of great importance, which is attributed to potential applications of SIMs or SMMs in high-density information storage and quantum processing.^{1–4} Mononuclear or binuclear Ln(III) compounds are very attractive. The simple systems are very convenient to study SIMs or SMMs systemically because of their easy tunability, coordination geometry, crystal field (CF) around the metal center, magnetic interactions between two spin carriers, and so on. Knowledge of the structure–magnetism correlations of Ln(III) SIMs or SMMs would be helpful for making a breakthrough in the thermal energy

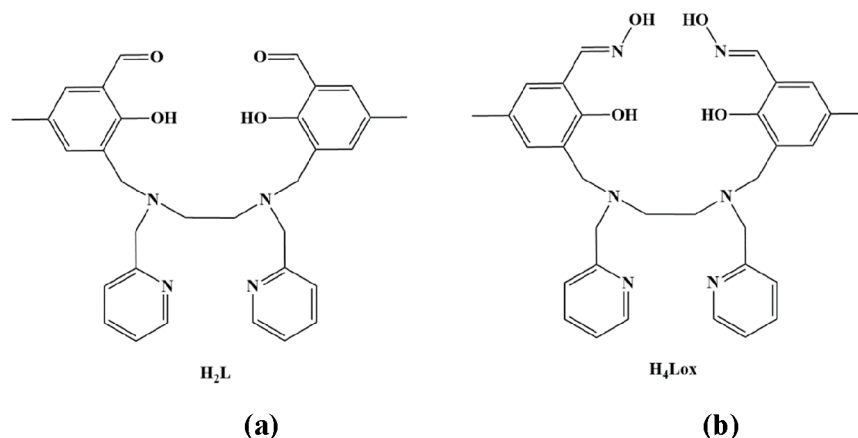
barriers of magnetization reversal (U_{eff}) and blocking temperatures (T_{B}). Regulation of SMMs is a big challenge because of the need to control various conditions, such as the pH, solvent, temperature, and ratio.^{2–10}

Remarkably, in situ Schiff base reactions have been observed during the synthesis processes of clusters.^{11–13} The new Schiff base ligand has many coordination points. Because of this, the target would be easily regulated. Especially, in situ Schiff base reaction can be applied to produce binuclear or cluster systems based on simpler structures.

Received: September 26, 2020

Published: January 2, 2021



Scheme 1. Molecular Structures of the Ligands H₂L (a) and H₄Lox (b)

Herein, a Schiff base ligand, *N,N'*-bis(2-hydroxy-5-methyl-3-formylbenzyl)-*N,N'*-bis(pyridin-2-ylmethyl)ethylenediamine (H₂L; Scheme 1a and Figures S1–S8),¹⁴ and two kinds of β -diketonate ligands, 1,3-bis(pyridin-2-yl)propane-1,3-dione (bppd) and 1-(4-chlorophenyl)-4,4,4-trifluoro-1,3-butanedione (ctbd), were selected to construct Dy(III) compounds for the following reasons: (1) It is highly probable that the N,O,N,O-based multichelating sites of the H₂L ligand would be inclined to shape a coordinate pocket and enclose one metal ion.¹⁵ (2) Some excellent Dy(III) SIMs with distinct coordination environments have been synthesized through these kinds of very similar ligands.^{16–18} (3) The β -diketonate ligand with a chelating coordination mode can be instrumental in constructing a stable mononuclear compound. (4) Dy(III) ions have been regularly used in building SIMs or SMMs with diverse polyhedral configurations and symmetries. A Dy(III) ion with a Kramers ground state of ⁶H_{15/2} possesses a large angular momentum, which is good for generating large Ising-type magnetic anisotropy.^{4,5,8–10} (5) What is more, the formyl groups of the H₂L ligand can be changed to hydroxyiminomethyl groups under certain conditions, resulting in the formation of a new polydentate ligand, *N,N'*-bis[2-hydroxy-5-methyl-3-(hydroxyiminomethyl)benzyl]-*N,N'*-bis(pyridin-2-ylmethyl)ethylenediamine (H₄Lox; Scheme 1b).¹⁴ Herein, two mononuclear compounds were obtained under solution reactions, namely, [Dy(L)(bppd)]·CH₃OH (1) and [Dy(L)(ctbd)] (3). Furthermore, the crystals of 1 or 3 were immersed in a mixed solution of DMF, CH₃CH₂OH, CH₂Cl₂, NH₂OH·HCl, and anhydrous Na₂CO₃. Finally, 1 and 3 were transformed into [Dy₂(H₂Lox)(bppd)₃]·8CH₃OH (2) and [Dy₂(H₂Lox)(ctbd)₃]·CH₃OH·C₄H₁₀O (4) through dissolution/precipitation processes, respectively. Compounds 2 and 4 exhibit binuclear structures. The formylbenzyl groups of H₂L in 1 and 3 were changed into (hydroxyiminomethyl)benzyl groups in 2 and 4, respectively. In situ ligand formation can be observed in the synthetic processes from mononuclear Dy(III) compounds to binuclear Dy(III) compounds. Moreover, the uniaxial anisotropy, magnetostructural correlation, and relaxation process were discussed through magnetic research and ab initio calculation.

EXPERIMENTAL SECTION

Materials and Instruction. The H₂L ligand was synthesized following a previous reference.¹⁴ 3-Bis(pyridin-2-yl)propane-1,3-dione (bppd), 1-(4-chlorophenyl)-4,4,4-trifluoro-1,3-butanedione (ctbd), Dy(NO₃)₃·6H₂O, triethylamine (Et₃N), *N,N*-dimethylformamide

(DMF), methanol (CH₃OH), ether (C₄H₁₀O), dichloromethane, NH₂OH·HCl, and anhydrous Na₂CO₃ were purchased from Sigma-Aldrich and used as received without further purification. The methods for structural characterization, thermal behavior, and magnetic measurement are given in the Supporting Information.

Synthesis of Compounds 1–4. **Synthesis of Compound [Dy(L)(bppd)]·CH₃OH (1).** H₂L (0.1 mmol, 0.0524 g), bppd (0.1 mmol, 0.0226 g), and Et₃N (0.1 mmol, 0.0102 g) were dissolved in 10 mL of a CH₃OH solution. The mixed solution was added to a CH₃OH solution (10 mL) of Dy(NO₃)₃·6H₂O (0.1 mmol, 0.0457 g) with stirring for 6 h. After that, the resultant mixture was filtered. By slow evaporation of CH₃OH into air at room temperature, some pale-yellow crystals of 1 were observed after several days. Yield: 39% [0.0137 g, based on the Dy(III) salts]. Anal. Calcd for C₄₆H₄₅DyN₆O₇ (956.38): C, 57.72; H, 4.71; N, 7.53. Found: C, 57.93; H, 4.79; N, 7.45. IR (KBr, cm⁻¹): 3438 (m), 2854 (m), 1650 (s), 1607 (s), 1535 (m), 1469 (s), 1412 (m), 1388 (m), 1351 (m), 1298 (s), 1263 (s), 1226 (m), 1188 (m), 1141 (m), 1063 (m), 1008 (w), 933 (w), 879 (m), 863 (m), 826 (m), 789 (w), 721 (m), 678 (w), 640 (m), 584 (w), 499 (w).

Synthesis of Compound [Dy₂(H₂Lox)(bppd)₃]·8CH₃OH (2). The crystals of 1 (0.1 mmol) were added to a mixed solution of 4:1 CH₃OH/DMF (10 mL). NH₂OH·HCl (0.0102 g, 0.1 mmol) and anhydrous Na₂CO₃ (0.1 mmol, 0.0102 g) were dissolved in 10 mL of a CH₃OH/dichloromethane solution. The solutions above were mixed and stirred for 30 h at room temperature. The crystals of 1 were dissolved. After that, the resultant mixture was filtered. By the slow evaporation of solvent molecules into air at room temperature, yellow block crystals of 2 were obtained after several weeks. Anal. Calcd for C₇₉H₉₃Dy₂N₁₂O₁₈ (1823.67): C, 54.98; H, 5.10; N, 9.21. Found: C, 54.94; H, 5.15; N, 9.17. IR (KBr, cm⁻¹): 3438 (m), 2060 (m), 1642 (s), 1550 (s), 1519 (m), 1480 (s), 1458 (m), 1408 (s), 1381 (s), 1306 (m), 1265 (m), 1225 (w), 1157 (w), 1025 (w), 940 (w), 804 (w), 863 (w), 756 (w), 725 (w), 693 (w), 610 (w), 523 (w).

Synthesis of Compound [Dy(L)(ctbd)] (3). The synthetic process of 3 is similar to that of 1. The bppd ligand (0.1 mmol, 0.0226 g) in 1 was changed to ctbd (0.1 mmol, 0.0251 g). Finally, pale-yellow block crystals of 3 were obtained after several days. Yield: 45% [0.0207 g, based on the Dy(III) salts]. Anal. Calcd for C₄₂H₃₇ClDyF₃N₄O₆ (948.71): C, 53.12; H, 3.90; N, 5.90. Found: C, 53.17; H, 3.94; N, 5.87. IR (KBr, cm⁻¹): 3443 (m), 2856 (m), 1650 (s), 1614 (s), 1572 (s), 1516 (w), 1467 (s), 1387 (m), 1351 (w), 1301 (s), 1263 (s), 1226 (m), 1193 (s), 1140 (m), 1095 (m), 1063 (m), 1014 (w), 948 (w), 910 (w), 879 (m), 863 (m), 826 (w), 793 (w), 763 (w), 718 (w), 647 (m), 586 (w), 499 (w).

Synthesis of Compound [Dy₂(H₂Lox)(ctbd)₃]·CH₃OH·C₄H₁₀O (4). A synthetic procedure similar to that for 2 was used to synthesize 4 except that a 4:1 CH₃OH/DMF solution (10 mL) was replaced by a 4:1:1 CH₃OH/C₄H₁₀O/DMF solution (10 mL). Finally, orange-yellow block crystals of compound 4 were obtained by the slow evaporation of solvent after several weeks. Anal. Calcd for

Table 1. Crystallographic Data and Structural Refinements for Compounds 1–4

	1	2	3	4
molecular formula	C ₄₆ H ₄₅ DyN ₆ O ₇	C ₇₉ H ₉₃ Dy ₂ N ₁₂ O ₁₈	C ₄₂ H ₃₇ ClDyF ₃ N ₄ O ₆	C ₆₅ H ₅₉ Cl ₃ Dy ₂ F ₉ N ₆ O ₁₂
fw	956.38	1823.67	948.71	1718.53
temperature (K)	293(2)	293(2)	293(2)	293(2)
cryst syst	monoclinic	monoclinic	monoclinic	monoclinic
space group	<i>P</i> 2 ₁ / <i>n</i>	<i>P</i> 2 ₁ / <i>c</i>	<i>P</i> 2 ₁ / <i>c</i>	<i>P</i> 2 ₁ / <i>n</i>
<i>a</i> (Å)	15.8427(3)	13.2072(12)	10.9905(5)	13.4189(12)
<i>b</i> (Å)	14.7700(2)	34.767(5)	10.8292(7)	22.4963(16)
<i>c</i> (Å)	18.9588(3)	17.250(2)	35.578(2)	23.249(2)
α (deg)	90	90	90	90
β (deg)	106.966(2)	96.645(10)	112.713(6)	102.999(10)
γ (deg)	90	90	90	90
<i>V</i> (Å ³)	4243.22(13)	7867.4(16)	3906.1(4)	6838.3(11)
<i>Z</i>	4	4	4	4
<i>D</i> _{calc} (g cm ⁻³)	1.497	1.540	1.613	1.669
<i>F</i> (000)	1940	4367	1900	3404
μ (mm ⁻¹)	9.901	11.107	11.444	13.405
θ_{\min} – θ_{\max} (deg)	3.209–67.064	3.601–64.983	2.690–67.250	3.502–65.998
reflns collected	21770	31687	13572	27317
GOF on <i>F</i> ²	1.043	0.942	1.004	1.063
<i>R</i> ₁ ^a / <i>wR</i> ₂ ^b [<i>I</i> > 2 σ (<i>I</i>)]	0.0450/0.1092	0.0858/0.1751	0.0555/0.0947	0.0847/0.1660
<i>R</i> ₁ / <i>wR</i> ₂ (all data)	0.0558/0.1162	0.2218/0.2549	0.1039/0.1168	0.1870/0.2178
CCDC	1947756	1947757	2024916	2024917

$$^a R_1 = \frac{\sum |F_o| - |F_c|}{\sum |F_o|}, \quad ^b wR_2 = \left[\frac{\sum w(F_o^2 - F_c^2)^2}{\sum w(F_o^2)^2} \right]^{1/2}.$$

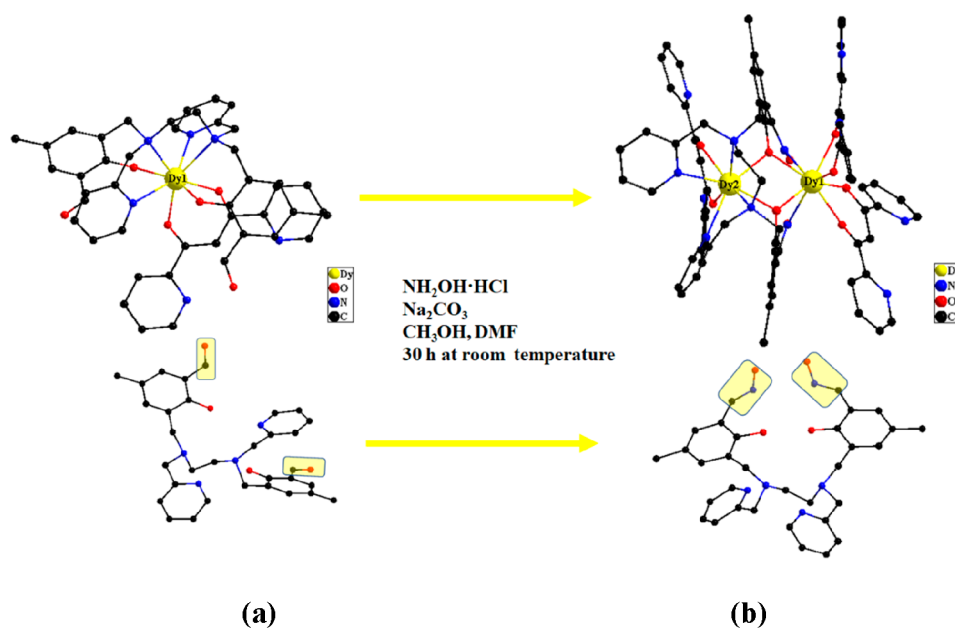


Figure 1. Crystal structures of compounds 1 (a) and 2 (b) showing general ligand configurations.

C₆₅H₅₉Cl₃Dy₂F₉N₆O₁₂ (1718.53): C, 45.39; H, 3.43; N, 4.89. Found: C, 45.33; H, 3.39; N, 4.95. IR (KBr, cm⁻¹): 3333 (m), 2842 (m), 1619 (s), 11589 (s), 1567 (m), 1521 (w), 1487 (m), 1467 (m), 1382 (m), 1265 (s), 1245 (w), 1191 (m), 1142 (m), 1088 (m), 1072 (m), 1010 (w), 854 (w), 801 (m), 662 (w), 586 (w), 555 (w), 476 (w), 439 (w).

Single-Crystal X-ray Diffraction Analysis. The SADABS¹⁹ and SHELXL-2018²⁰ programs were used in data analysis. Crystal data and structure refinements were displayed in the Supporting Information. Other details of the crystal data and refinement statistics are given in Table 1. The selected bond lengths and angles are listed in Table S1.

RESULTS AND DISCUSSION

Crystal Structures. The synthetic processes for 1–4 are shown in Figures 1 and S9. Compounds 2 and 4 were synthesized by using compounds 1 and 3, respectively. The crystals of 1 were dissolved in a mixed solution of DMF, CH₃CH₂OH, CH₂Cl₂, NH₂OH·HCl, and anhydrous Na₂CO₃. The solution above was stirred for about 30 h at room temperature. Finally, some yellow crystals of 2 were observed at the bottom of beaker after several weeks. Obviously, the crystals of 1 were transformed into 2 through a dissolution/precipitation process. Meanwhile, the crystals of 3 were used to synthesize compound 4. The 4:1 CH₃OH/DMF solution (10

mL) in **2** was replaced by 4:1:1 CH₃OH/C₄H₁₀O/DMF solution (10 mL) in the synthetic process of **4**. High-quality crystals of **4** without impurities could be obtained when C₄H₁₀O was introduced into the synthetic process of compound **4**. Compounds **1–4** were fully characterized through powder X-ray diffraction (Figures S10–S13), elemental analysis, IR spectroscopy (Figures S14–S17), thermal analysis (Figures S18–S21) and single-crystal X-ray diffraction (Tables 1 and S1) techniques. Meanwhile, the compositions of compounds **1–4** were determined by these measurements. The results of structural analyses reveal that **1** and **4** crystallize in the monoclinic space group $P2_1/n$ (Table 1). **2** and **3** crystallize in the monoclinic space group $P2_1/c$. Compounds **1** and **3** exhibit similar mononuclear structures (Figures 1 and S9). A Dy(III) ion in **1** is coordinated through one deprotonated L²⁻ ligand and one negative β -diketonate ligand. Dy(III) ions in **1** and **3** display eight-coordinated environments. One CH₃OH solvent guest is found to reside in **1** (Figure S22). No solvent molecules are observed in **3**. However, compounds **2** and **4** display binuclear structures (Figures 1 and S9). 2-Dy1 or 4-Dy1 ions locate in a pocket formed by two benzaldoxime N atoms and two bridged phenol O atoms of the H₂Lox²⁻ ligand as well as four chelated O atoms of two β -diketonate ligands. Eight-coordinated 2-Dy2 or 4-Dy2 ions are surrounded by two ethylenediamine N atoms, two pyridine N atoms, and two bridged phenol O atoms of the H₂Lox²⁻ ligand as well as two chelated O atoms of one β -diketonate ligand, respectively. The formyl groups of H₂L in **1** and **3** were changed to the hydroxyiminomethyl groups of H₄Lox in **2** and **4** under certain conditions, respectively. The lattice solvent molecules are found in the molecular structures of **2** and **4**. The Dy(III)–O bond lengths are in the ranges 2.229(3)–2.322(3) Å for **1**, 2.237(10)–2.380(9) Å for **2**, 2.230(5)–2.346(5) Å for **3**, and 2.247(8)–2.314(10) Å for **4**, respectively (Table S1). The Dy(III)–N bond lengths are in the ranges 2.590(4)–2.628(3) Å for **1**, 2.531(12)–2.601(13) Å for **2**, 2.560(6)–2.632(6) Å for **3**, and 2.550(13)–2.566(12) Å for **4**, respectively. The shortest Dy(III)–O distances are 2.229(3) Å [Dy(III)–O2], 2.237(10) Å [Dy(III)–O7], 2.230(5) Å [Dy(III)–O5], and 2.247(8) Å [Dy(III)–O7] in **1–4**, respectively. In **1–4**, the average distances of the Dy(III)–O bonds are 2.285, 2.396, 2.292, and 2.297 Å, while the average Dy(III)–N lengths are 2.614, 2.569, 2.597, and 2.562 Å, respectively. Obviously, the shortest Dy(III)–O bond length is observed in **1**. However, the Dy(III)–N distances for **1** and **2** are longer than those for **3** and **4**, respectively. The units in **1–4** are well-separated, and the nearest intermolecular Dy(III)⋯Dy(III) distances are 9.1198(5), 7.9204(17), 9.8662(8), and 9.1732(12) Å, respectively. In compound **1**, formation of the O–H⋯O hydrogen bond with O7–H7A⋯O5 lead to bond distances of 0.821 and 2.285 Å (Figure S22), respectively. The hydrogen bond angle is 117.75°. The metal centers in the dinuclear cores of **2** and **4** are bridged by two phenol O atoms (O4 and O9 in **2**; O7 and O9 in **2**) of one H₂Lox²⁻ ligand (Figures 2 and S23), with the Dy(III)⋯Dy(III) distances being 3.8843(14) and 3.8223(12) Å, respectively. The Dy(III)–O–Dy(III) angles are 115.9(4)° [Dy(III)–O4–Dy(III)] and 113.5(4)° [Dy(III)–O9–Dy(III)] in **2** as well as 113.5(3)° [Dy(III)–O7–Dy(III)] and 113.2(4)° [Dy(III)–O9–Dy(III)] in **4**, respectively.

These configurations of the Dy(III) centers in **1–4** were analyzed through the SHAPE 2.1 software (Table S2).^{21,22} Compounds **1** and **3** belong to approximately triangular

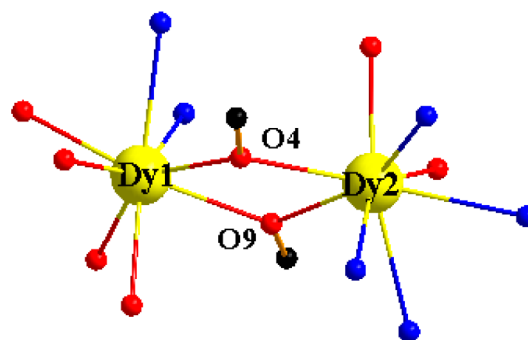


Figure 2. Metal centers in the dinuclear core of **2** are bridged by two phenol O atoms (O4 and O9) of one H₂Lox²⁻ ligand.

dodecahedron (D_{2d}) configurations. The Dy1 and Dy2 centers in **2** and **4** closely pertain to a square antiprism (D_{4d}) configuration with a continuous shape measure (CShM) parameters of 0.714 (2-Dy1) and 0.833 (4-Dy1) as well as an approximate triangular dodecahedron (D_{2d}) configuration with CShM parameters of 1.185 (2-Dy2) and 1.182 (4-Dy2), respectively. The polyhedra of the Dy(III) centers for **1–4** can be observed in Figures 3 and S24.

Magnetic Properties. Powder X-ray diffraction patterns were measured (Figures S10–S13). The results indicate that these experimental patterns are in accordance with the corresponding calculated ones to verify the phase purity of **1–4**. Direct-current (dc) magnetic susceptibility data of **1–4** were carried out from 2 to 300 K under a 1000 Oe dc field (Figure 4). The $\chi_M T$ values for **1** and **3** are 14.35 and 14.29 cm³ K mol⁻¹ at 300 K, respectively, which are in agreement with the theoretical value of a noninteracting Dy(III) ion ($S = 5/2$, $L = 5$, $g = 4/3$, and $^6H_{15/2}$).²³ For compounds **2** and **4**, the $\chi_M T$ values are 28.07 and 28.73 cm³ K mol⁻¹ at 300 K, respectively. The two values are close to the theoretical value of 28.34 cm³ K mol⁻¹ for two noninteracting Dy(III) ions in the $^6H_{15/2}$ ground state.²³ Upon cooling, the $\chi_M T$ values of **1** and **3** slightly decrease in the high-temperature range. Furthermore, the curves degrade rapidly at low temperature. At 2.0 K, the values in **1** and **3** are 8.55 and 12.07 cm³ K mol⁻¹, respectively, strongly implying the presence of magnetic blocking. As the temperature is lowered, the $\chi_M T$ products of **2** and **4** decrease gradually as thermal depopulation of the Stark sublevels of the Dy(III) ion.²³ The minimum values are 22.76 cm³ K mol⁻¹ for **2** at 7.0 K and 22.85 cm³ K mol⁻¹ for **4** at 10.0 K. The $\chi_M T$ values of **2** and **4** then increase sharply to values of 23.41 and 23.79 cm³ K mol⁻¹ at 2.0 K, respectively. The process results from the intramolecular ferromagnetic coupling for **2** and **4**.

Field-dependent magnetization of **1–4** was carried out at 2.0 K (Figure 5). The values of **1–4** increase fast at weak fields and then increase slowly. The magnetization values of **1–4** increase to 6.08, 11.39, 5.00, and 10.68 N β at 70 kOe, respectively. These values at 70 kOe are lower than the expected saturation values of 10 or 20 N β , which are mainly attributed to strong magnetic anisotropy.²³ The magnetic hysteresis loops were examined for **1–4**. Butterfly-shaped hysteresis loops are obviously open from 2 to 5 K in **1** (Figure 6a). A weak butterfly-shaped hysteresis loop can be observed at 2 K in **3** (Figure 6b). However, magnetic hysteresis loops cannot be found in compounds **2** and **4**.

The temperature dependence of alternating-current (ac) susceptibilities for **1–4** was carried out under a 0 Oe dc field

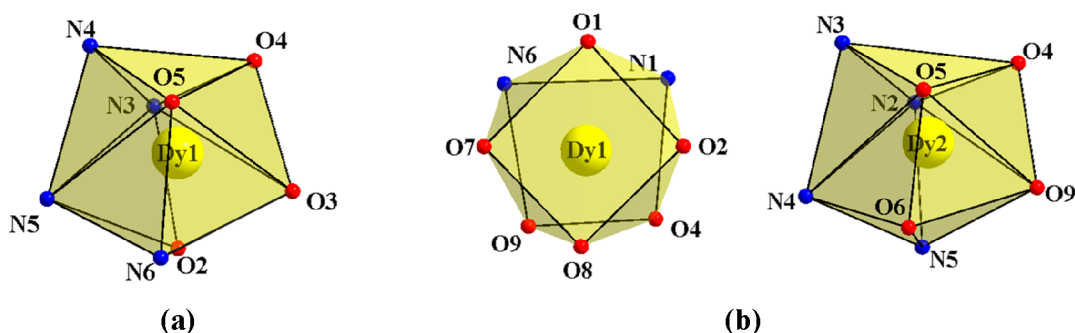


Figure 3. Local coordination geometries of the Dy(III) ions for 1 (a) and 2 (b).

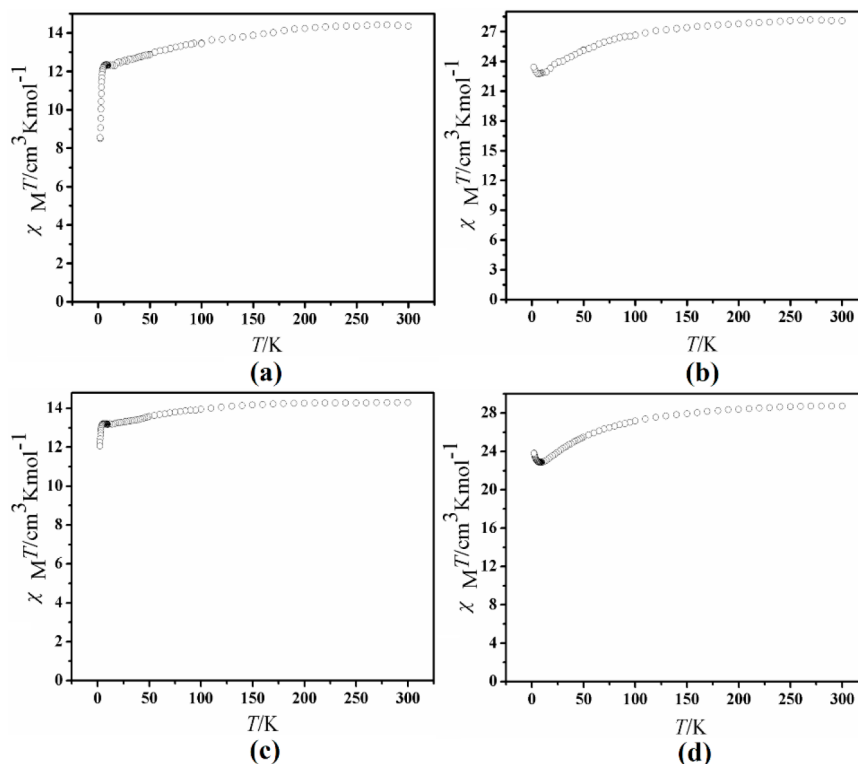


Figure 4. Temperature dependence of $\chi_M T$ measured at 1 kOe for 1–4 (a–d), respectively.

(Figures S25–S28). For 1, out-of-phase (χ'') susceptibilities show obvious temperature dependence (Figure S25). Their peaks are in good shape, indicating typical SMM behaviors. No peak data can be observed above 2.0 K in compounds 2–4 (Figures S26–S28). The χ' and χ'' products of 1–4 increase as the temperature decreases. The χ' and χ'' values rise again in 1 below 7.5 K, revealing the appearance of quantum tunneling of magnetization (QTM). The phenomenon is often found in SMMs. To restrain QTM, the temperature dependence of ac susceptibilities for 2 was measured with a 1500 Oe dc field (Figure S29). The significant peaks demonstrate field-induced slow magnetic relaxation behavior.

Besides, the frequency dependence of ac susceptibilities in 1–4 was measured, as seen in Figures 7–10. Compounds 1 and 3 show frequency dependencies based on observable χ' and χ'' signals (Figures 7 and 9), respectively. The peaks of the χ'' susceptibilities for 1 and 3 smoothly shift from the medium-frequency region to the high-frequency region with rising temperature. The variable frequencies on the ac susceptibility measurement of 2 were performed at 2.2 K under a wide range

of applied dc fields (Figure S30). Strikingly, 1200 or 1500 Oe is the optimal field (H_{op}), which results in strong relaxation phase. Therefore, the frequency-dependent ac magnetic susceptibilities were carried out in the range from 2.0 to 5.5 K under a 1200 Oe dc field (Figure 8) as well as from 2.0 to 7.0 K under a 1500 Oe dc field in 2 (Figure S31). Both the χ' and χ'' signals of compound 2 exhibit frequency dependencies. The χ'' peaks present two relaxation processes, attributed to the fast relaxation (FR) and slow relaxation (SR) processes, respectively. The FR process in compound 2 may result from one main reason: QTM is enhanced by dipolar interactions between the Dy ions, which can be partly suppressed by the applied field. Additionally, it is also possible that the two relaxation processes came from the two different Dy(III) ions.^{23f} Compound 4 shows very weak χ'' signals under a 0 Oe dc field (Figure S32). The variable frequencies on the ac susceptibility measurement in 4 were carried out at 2.2 K under a wide range of applied dc fields (Figure S33). Obviously, a H_{op} value of 800 Oe results in a strong relaxation phase in the high-frequency region. Furthermore, ac magnetic

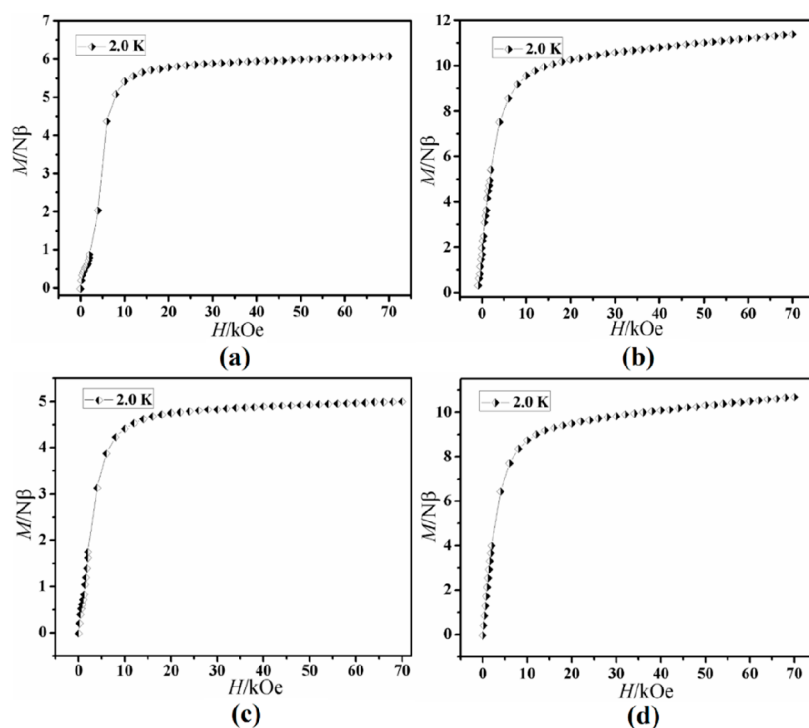


Figure 5. $M(H)$ plots for 1–4 (a–d), respectively.

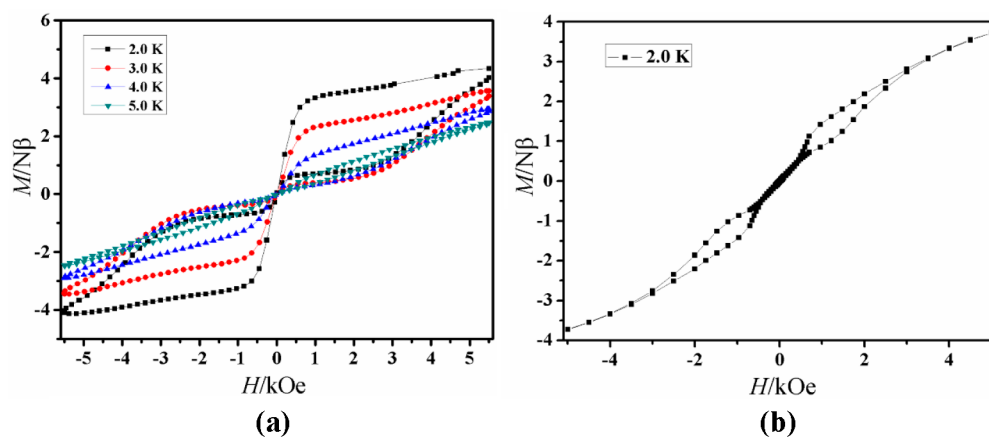


Figure 6. Magnetic hysteresis loops for 1 (a) and 3 (b).

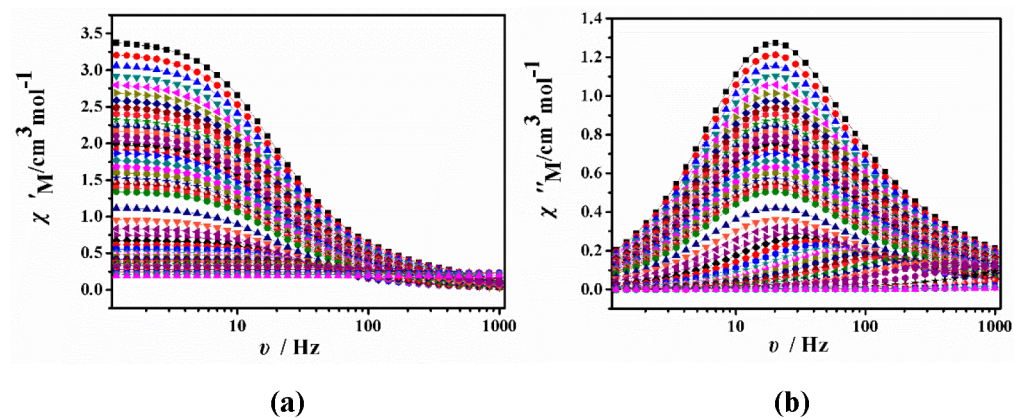


Figure 7. Plots of the χ' (a) and χ'' (b) ac susceptibilities from 2.0 to 35.0 K for 1 under a 0 Oe dc field.

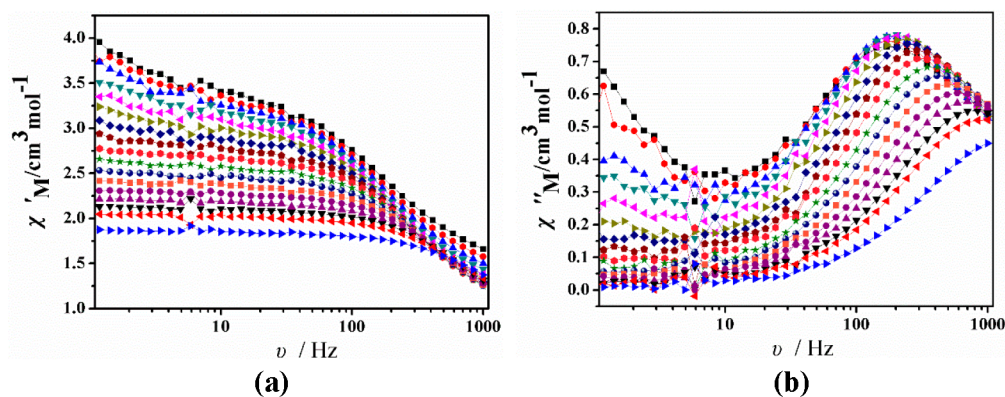


Figure 8. Plots of the χ' (a) and χ'' (b) ac susceptibilities from 2.0 to 7.0 K for 2 under a 1200 Oe dc field.

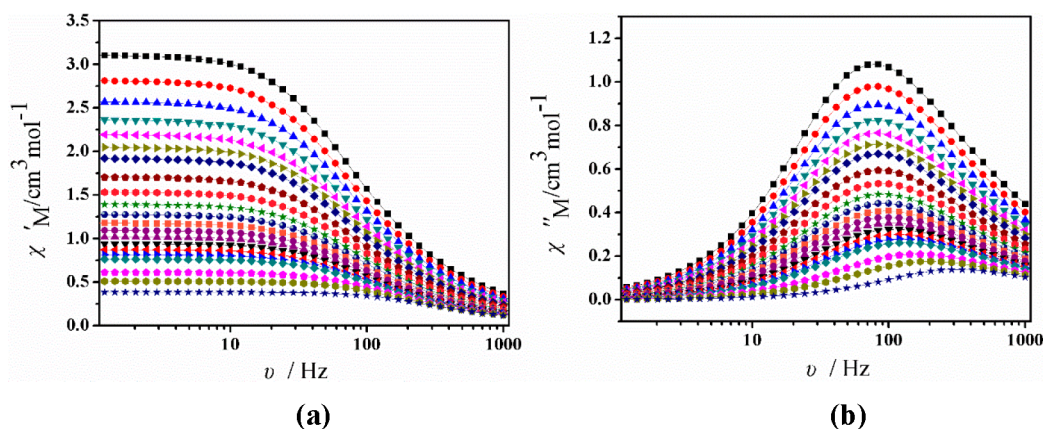


Figure 9. Plots of the χ' (a) and χ'' (b) ac susceptibilities from 2.0 to 16.0 K for 3 under a 0 Oe dc field.

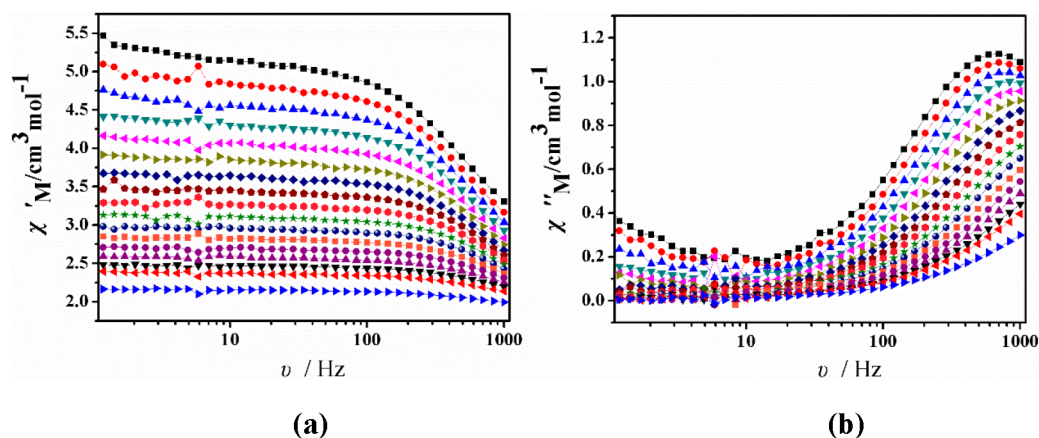


Figure 10. Plots of the χ' (a) and χ'' (b) ac susceptibilities from 2.0 to 5.5 K for 4 under a 800 Oe dc field.

data for 4 were collected in the range from 2.0 to 5.5 K under a 800 Oe dc field (Figure 10). The frequency dependencies were observed in the χ' and χ'' components of compound 4. Meanwhile, the FR and SR processes were also found in 4. A similar phenomenon can be seen in compound 2.^{23f}

The Cole–Cole plots of 1 and 3 based on the frequency-dependent ac susceptibilities exhibit good semicircular shapes (Figures 11 and 12). The Cole–Cole plots of 2 and 4 present two relaxation phases corresponding to the FR and SR processes (Figures S34–S36). When the corresponding data of 1 and 3 are fitted with a generalized Debye model, the parameter α can be obtained in the ranges of 0.064–0.173

(Figure S37 and Table S3) and 0.102–0.186 (Figure S38 and Table S4), respectively, indicating a narrow distribution of relaxation times for a single relaxation process. This narrow distribution indicates that magnetic relaxation can be well described by a single relaxation time parameter τ in 1 or 3. The relaxation times of 1 and 3 at high temperatures obey an Arrhenius law [$\tau = \tau_0 \exp(U_{\text{eff}}/kT)$] with effective energy barriers of $U_{\text{eff}} = 171.7$ K and $\tau_0 = 1.28 \times 10^{-7}$ s as well as $U_{\text{eff}} = 22.7$ K and $\tau_0 = 9.29 \times 10^{-5}$ s, respectively (Figures 13 and 14). The $\ln(\tau)$ versus $1/T$ plots in 1 and 3 exhibit some curvature. The overall dynamics cannot be properly modeled based on the Orbach mechanism. Therefore, the total

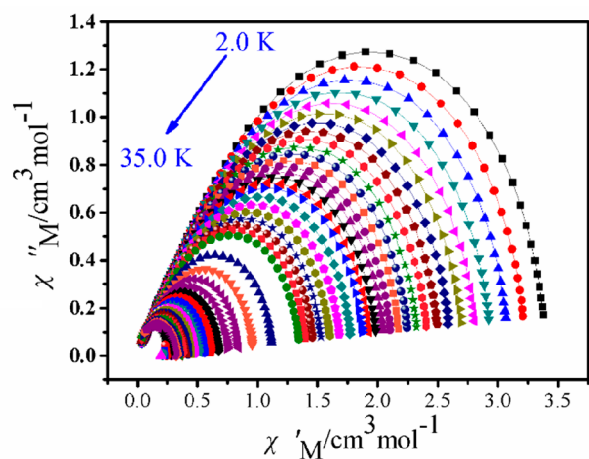


Figure 11. Cole–Cole plots for **1** from 2.0 to 35.0 K under a 0 Oe applied dc field.

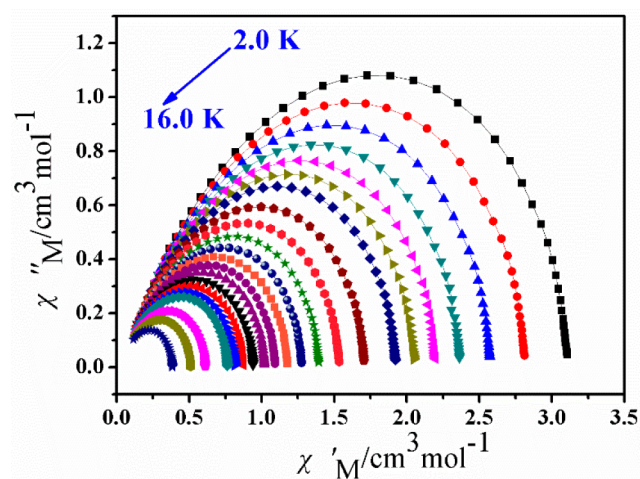


Figure 12. Cole–Cole plots for **3** from 2.0 to 16.0 K under a 0 Oe applied dc field.

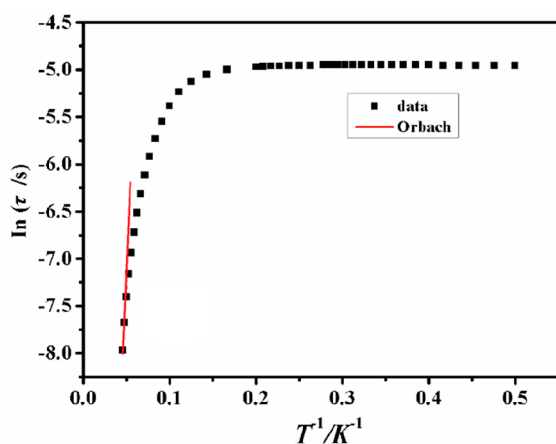


Figure 13. Fitting of the frequency dependence of relaxation times under a 0 Oe dc field for compound **1**.

relaxation rates were fitted through the Orbach, Raman, and QTM processes (Figures S39 and S40), resulting in an effective energy barriers of $U_{\text{eff}} = 247.3$ K in **1** and $U_{\text{eff}} = 78.0$ K in **3**. The details can be seen in Table S5.

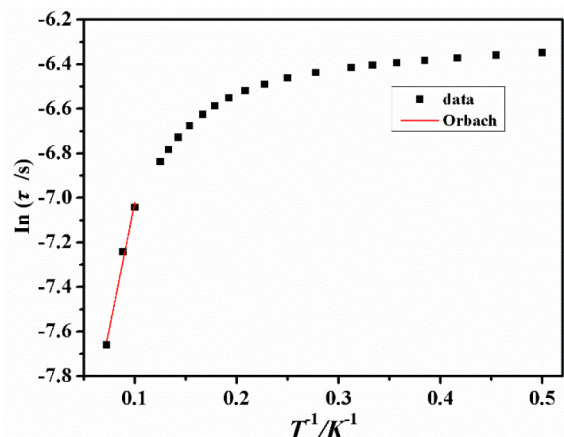


Figure 14. Fitting of the frequency dependence of relaxation times under a 0 Oe dc field for compound **3**.

Theoretical Analysis and Structure–Property Relationship.

In order to interpret the magnetic anisotropy and relaxation of the systems here, electronic structure calculations, based on multiconfigurational methods including spin–orbit coupling, were performed. The ab initio calculations were conducted via a procedure of CASSCF/RASSI-SO/SINGLE ANISO.^{24–32} All of the calculations were carried out with the code of MOLCAS@UU, a free version of MOLCAS 8.0^{33,34} for academic users. The details of the computations are included in the Supporting Information.

For **1** and **3**, the crystal structure was used directly. For **2** and **4** of dinuclear geometry, each of the paramagnetic Dy(III) ions was replaced by one diamagnetic Lu(III) to give mononuclear models for ab initio calculation. These models are denoted as **2-Dy1**, **2-Dy2**, **4-Dy1**, and **4-Dy2** hereafter.

In principle, the microscopic states of the Kramers system, e.g., **1** and **2** here, are grouped into various 2-fold degenerate states, called as Kramers doublets (KDs). Each KD could be uniquely associated with a pseudospin of $1/2$, i.e., $\hat{S} = 1/2$.^{31,32,35,36} Thus, the principal values of the g matrix of this pseudospin provide an univocal description on the related KD.^{8,9,13} With accurate ab initio results, analysis based on these g values is reliable and widely accepted in the field of Ln-based SIM.^{24,31,32,35,37–44}

The dinuclear **2** and **4** are non-Kramers Ln-based systems. The 4f electrons of Ln ions are strongly localized, and, hence, the exchange interaction between Ln ions is usually accepted to be very weak.^{24,35,41} In comparison, the magnetic dipolar interaction between Ln ions is usually stronger than the exchange interaction. However, even the sum of these two interion interactions is quite weaker than the local CF of an individual Ln ion.³⁵ Thus, the final electronic structure of either **2** or **4** is dominated by the sum of the local CF levels of constituent mononuclear Kramers Ln fragments.^{35,38,41} Finally, these local CF levels will be expanded into bands due to the weak interion interaction.

The electronic structure of a dinuclear Ln compound includes groups of energy levels. The intergroup energy differences are mainly determined by the local CF of various Ln ions. However, the small intragroup energy difference is mainly determined by the weak exchange and dipolar interactions. Thus, the lowest doublets of **2** and **4** are well separated from other doublets, and they mainly arise from the

interaction between ground-state KDs of individual Ln fragments.³⁵

To observe slow magnetic relaxation, the relaxation rate ought to be slow enough to be monitored by an experimental apparatus. In Ln-based SMMs, different pathways of relaxation exist at the same time,^{35,37–39,45} and, thus, the final relaxation rate has contributions from all of the existing pathways. The dominance of one single pathway across a wide temperature range is rare in Ln-based SMMs.^{37,38,45} This is one important reason for the complexity of Ln-based SMMs.

The relaxation pathways could be grouped into spin–lattice pathways⁴³ and QTM.⁴⁴ Generally, the rate of QTM (τ_{QTM}^{-1}) within the ground-state doublet dominates in the region of low temperature, so that τ_{QTM}^{-1} could be taken as the lower limit of the total relaxation rate.⁴⁵ Thus, the necessary condition for the zero-field SMM is that τ_{QTM}^{-1} of the ground state is slow enough.^{38,45,46} Clearly, the key parameter characterizing QTM is just τ_{QTM}^{-1} or its reciprocal QTM time τ_{QTM} .

A general equation for theoretical prediction of τ_{QTM}^{-1} has been given previously (eq 1a).⁴⁵ For Kramers system under a 0 Oe dc field, the tunnel splitting (Δ_{tun}) and energy bias (ϵ_{bias}), which are necessary for the prediction of τ_{QTM}^{-1} , are provided by Zeeman interaction, as shown in eqs 1b and 1c. Under the assumption of an isotropic internal magnetic field, a working equation to predict τ_{QTM}^{-1} of a Kramers SIM (eq 1d) has been given, and it shows reliable accuracy.^{45,47}

$$\tau_{\text{QTM}}^{-1} = \frac{2\Delta_{\text{tun}}^2}{h(\epsilon_{\text{bias}}^2 + 4\Delta_{\text{tun}}^2)^{1/2}} \quad (1a)$$

$$\Delta_{\text{tun}} = \frac{1}{2}[\beta(g_X^2 B_X^2 + g_Y^2 B_Y^2)^{1/2}] \quad (1b)$$

$$\epsilon_{\text{bias}} = \beta B_Z g_Z \quad (1c)$$

$$\tau_{\text{QTM}}^{-1} = \frac{\beta B_{\text{ave}}}{h} \frac{g_{XY}^2}{2(g_{XY}^2 + g_Z^2)^{1/2}}, \quad (1d)$$

$$g_{XY} = (g_X^2 + g_Y^2)^{1/2}$$

It needs to indicate that the dominating pathways in the high-temperature region are the spin–lattice ones, e.g., the Orbach and Raman pathways, rather than QTM. The most popular parameter describing spin–lattice relaxation is the effective magnetic reversal barrier (U_{eff}).^{44,48,49} Thus, good SMMs could be concisely described as the ones of simultaneous achievement of both long τ_{QTM} and high U_{eff} .⁴⁵ However, the original definition of U_{eff} comes from the Arrhenius rule between the relaxation rate and temperature.⁵⁰ Among the various pathways of magnetic relaxation, this rule is only obeyed by the Orbach one. Thus, the importance of U_{eff} should not be overestimated because it is actually phenomenological.

With the principal g values obtained from ab initio calculations (Table 2), τ_{QTM} is predicted for the compounds here. In the cases of SIMs 1 and 3, theoretical τ_{QTM} ($\tau_{\text{QTM}}^{\text{theo}}$) is consistent with the experimental values ($\tau_{\text{QTM}}^{\text{exp}}$) because they are within the same order of magnitude, i.e., 0.1435×10^{-1} s versus 0.720×10^{-2} s for 1 and 0.5064×10^{-2} s versus 0.180×10^{-2} s for 3. Theoretical predictions are also consistent with the experimental observation in that τ_{QTM} of 1 is longer than that of 3. In other words, QTM of 1 is weaker than that of 3.

Table 2. Ab Initio Computed Relative Energies (cm^{-1}), Principal Values of the g Tensors, and Theoretical and Experimental QTM Times ($\tau_{\text{QTM}}^{\text{theo}}$ and $\tau_{\text{QTM}}^{\text{exp}}$ in Seconds) of the Compounds Studied in This Work

		1	2-Dy1	2-Dy2	
KD ₀	<i>E</i>	0.000	0.000	0.000	
	<i>g_Z</i>	19.9067	18.2784	18.6767	
	<i>g_X</i>	0.1222×10^{-2}	0.1445	0.2422	
	<i>g_Y</i>	0.1861×10^{-2}	0.3487	0.7407	
	<i>g_{XY}</i>	0.2226×10^{-2}	0.3774	0.7793	
	$\tau_{\text{QTM}}^{\text{theo}}$	0.1435×10^{-1}	0.4585×10^{-6}	0.1100×10^{-6}	
	$\tau_{\text{QTM}}^{\text{exp}}$	0.720×10^{-2}			
KD ₁	<i>E</i>	207.803 (171.8) ^a	52.846	78.604	
	<i>g_Z</i>	17.0215	14.3378	12.8343	
	<i>g_X</i>	0.7760×10^{-1}	0.1006×10^1	0.2788×10^1	
	<i>g_Y</i>	0.9773×10^{-1}	0.1190×10^1	0.3625×10^1	
	<i>g_{XY}</i>	0.1248	0.1559×10^1	0.4573×10^1	
	<i>E</i>	366.407	112.479	118.850	
KD ₂	<i>g_Z</i>	11.4018	11.4425	11.2489	
	<i>g_X</i>	0.2283×10^1	0.2170×10^1	0.1979×10^1	
	<i>g_Y</i>	0.4975×10^1	0.3289×10^1	0.3756×10^1	
	<i>g_{XY}</i>	0.5474×10^1	0.3940×10^1	0.4245×10^1	
	<i>E</i>	413.341	173.646	163.503	
	<i>g_Z</i>	0.1685	2.5208	12.7454	
KD ₃	<i>g_X</i>	0.9526×10^1	0.8512×10^1	0.2584×10^1	
	<i>g_Y</i>	0.7006×10^1	0.6378×10^1	0.2921×10^1	
	<i>g_{XY}</i>	0.1182×10^2	0.1064×10^2	0.3900×10^1	
			3	4-Dy1	4-Dy2
	KD ₀	<i>E</i>	0.000	0.000	0.000
		<i>g_Z</i>	19.9023	18.1217	19.1034
<i>g_X</i>		0.2228×10^{-2}	0.3377×10	0.2094×10^{-1}	
<i>g_Y</i>		0.3013×10^{-2}	0.1016×10^1	0.4208×10^{-1}	
<i>g_{XY}</i>		0.3747×10^{-2}	0.1071×10^1	0.4701×10^{-1}	
$\tau_{\text{QTM}}^{\text{theo}}$		0.5064×10^{-2}	0.5654×10^{-7}	0.3089×10^{-4}	
	$\tau_{\text{QTM}}^{\text{exp}}$	0.180×10^{-2}			
KD ₁	<i>E</i>	209.543 (54.2)	54.210	89.161	
	<i>g_Z</i>	17.0373	11.7906	14.6430	
	<i>g_X</i>	0.5764×10^{-1}	0.3060×10^1	0.4965×10	
	<i>g_Y</i>	0.6593×10^{-1}	0.5216×10^1	0.9371×10	
	<i>g_{XY}</i>	0.6593×10^{-1}	0.6048×10^1	0.1060×10^1	
	<i>E</i>	407.609	89.537	139.195	
KD ₂	<i>g_Z</i>	13.7086	10.0937	12.0463	
	<i>g_X</i>	0.7278×10	0.3410×10	0.1168×10	
	<i>g_Y</i>	0.9439×10	0.3704×10^1	0.1196×10^1	
	<i>g_{XY}</i>	0.1192×10^1	0.3720×10^1	0.1202×10^1	
	<i>E</i>	511.923	120.607	202.428	
	<i>g_Z</i>	12.6118	13.2062	9.2971	
KD ₃	<i>g_X</i>	0.3513×10^1	0.2580×10^1	0.1133×10^1	
	<i>g_Y</i>	0.5596×10^1	0.4044×10^1	0.3369×10^1	
	<i>g_{XY}</i>	0.6607×10^1	0.4797×10^1	0.3554×10^1	

^aThe values of experimentally fitted U_{eff} are shown in parentheses.

In principle, the $\tau_{\text{QTM}}^{\text{theo}}$ values of 2 and 4 in Table 2 are theoretical predictions for their constituent mononuclear fragments rather than the true dinuclear compounds. As shown above, the electronic structures of 2 and 4 are mainly determined by these mononuclear fragments. Thus, we assume that the properties of the constituent fragments could represent the essential part of the properties of their parent dinuclear compounds. For 2 and 4, τ_{QTM} is theoretically predicted to be within the range 10^{-8} – 10^{-5} s (Table 2). These are quite short QTM times (or fast QTM rates equally), which

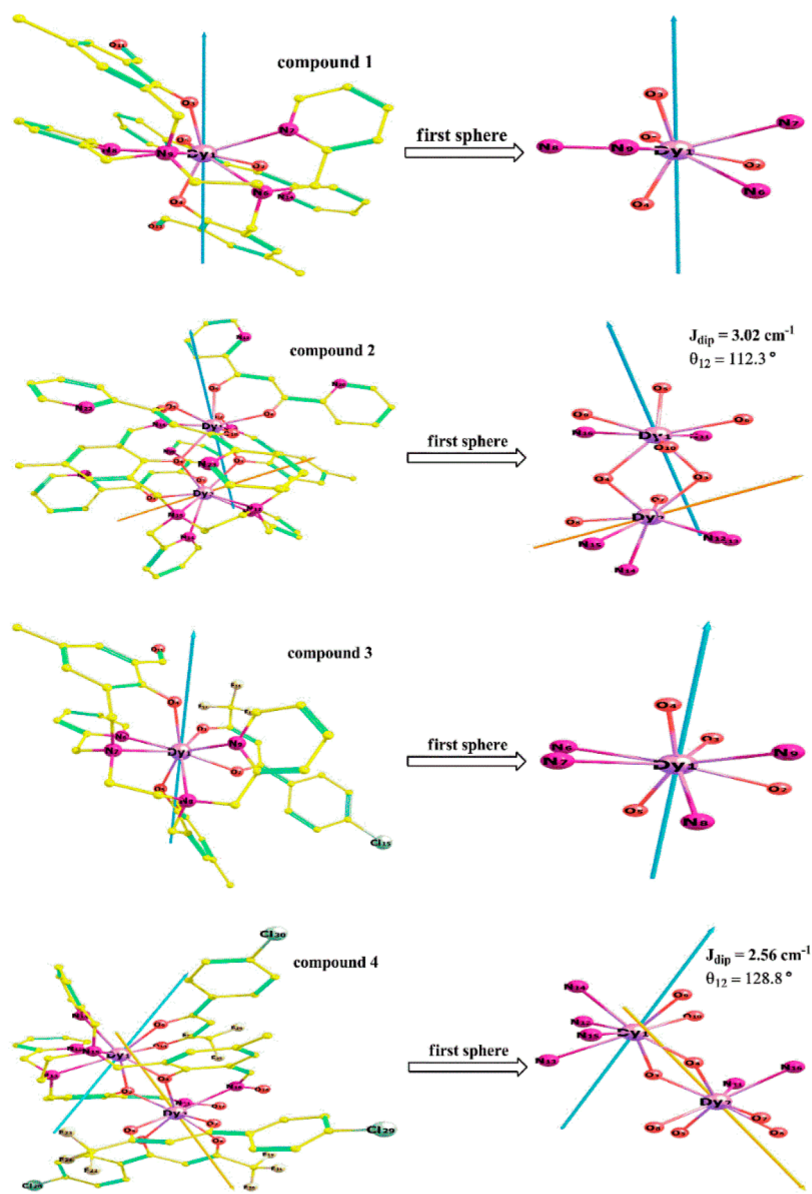


Figure 15. Directions of the ab initio magnetic easy axes of the ground-state KDs of the compounds here.

are hard to catch based on the current experimental apparatus. As shown above, under a 0 Oe dc field, neither **2** nor **4** demonstrates a peak in their ac susceptibility signals. These experimental observations mean that magnetic relaxation of **2** and **4** is very fast. Thus, our theoretical prediction is also consistent with the experiments in **2** and **4**. According to the results of the constituent fragments, the dipolar parameters J_{dip} are calculated to be 3.02 and 2.56 cm^{-1} for **2** and **4**, respectively. These theoretical results are consistent with the experimental observation of weak ferromagnetic (FM) coupling in both **2** and **4**.

Furthermore, **1** is theoretically predicted to have the weakest QTM among the compounds here, and this prediction is also in line with the observation that the SMM properties of **1** are the best here because it is the only one that clearly shows a peak in the imaginary part of the ac signal under a 0 Oe dc field and its opening in the magnetic hysteresis loop is wider.

Under the dominance of the Orbach pathway, U_{eff} could be close to the energy of a given excited state. As shown in Figure S41, the spin–lattice relaxation here proceeds via the first

excited-state KD, i.e., KD_1 . However, the residual ground-state QTM, represented by the red arrow connecting the ground-state KD (Figure S41), as well as the Raman pathway exclude the ideal dominance of Orbach one. Therefore, U_{eff} fitted from the experimental data, is clearly lower than the ab initio energy of KD_1 (Table 2). **1** is the one for which the experimentally fitted U_{eff} is closest to the energy of KD_1 among the compounds here. This might be due to the fact that the ground-state QTM of **1** is the weakest.

Because of the oblate electron density of the ground-state multiplet of the Dy(III) ion,^{51–57} a suitable electronic structure for a promising Dy SIM could be analyzed via an electrostatic route.^{39,51–54} This means that the electrostatic repulsion (ESP) along the easy axis should be as strong as possible. The ab initio magnetic easy axes are shown in Figure 15. Therefore, the axial atoms could be defined as the ones lying closest to the easy axis within the first sphere (Table 3).

With the atomic charges and lengths to the central Dy(III) ion (Table 3), we could estimate the ESP along the axial direction at a semiquantitative level.^{39,52–54} As shown in Table

Table 3. Atomic Charges (|e|) from Ab Initio Calculations, Related Dy–O/N Bond Lengths (Å), and Angles θ (deg) with Respect to the Magnetic Easy Axes of the Ground-State KDs of the Atoms in the First Sphere

Compound 1								
	O ₃ -a ^a	O ₄ -a	O ₂	O ₅	N ₆	N ₇	N ₈	N ₉
charge	−0.887	−0.880	−0.760	−0.742	−0.288	−0.329	−0.330	−0.301
Dy–O/N	2.228	2.267	2.322	2.320	2.628	2.616	2.590	2.621
θ^b	10.1	18.7						
ESP(ax) ^c	0.750							
Compound 2-Dy1								
	O ₃ -a	O ₅ -a	O ₄	O ₆	O ₉	O ₁₀	N ₁₁	N ₁₆
charge	−0.8171	−0.737	−0.766	−0.769	−0.722	−0.759	−0.130	−0.192
Dy–O/N	2.262	2.311	2.376	2.276	2.243	2.340	2.574	2.555
θ	17.8	33.1						
ESP(ax)	0.640							
Compound 2-Dy2								
	O ₃ -a	O ₈ -a	O ₄	O ₇	N ₁₂	N ₁₃	N ₁₄	N ₁₅
charge	−0.806	−0.738	−0.802	−0.773	−0.305	−0.360	−0.356	−0.299
Dy–O/N	2.342	2.280	2.280	2.288	2.601	2.562	2.592	2.547
θ	35.9	21.7						
ESP(ax)	0.623							
Compound 3								
	O ₄ -a	O ₅ -a	O ₂	O ₃	N ₆	N ₇	N ₈	N ₉
charge	−0.871	−0.868	−0.689	−0.679	−0.340	−0.305	−0.293	−0.344
Dy–O/N	2.247	2.230	2.342	2.345	2.560	2.632	2.629	2.565
θ	11.3	17.1						
ESP(ax)	0.743							
Compound 4-Dy1								
	O ₃ -a	O ₉ -a	O ₄	O ₁₀	N ₁₂	N ₁₃	N ₁₄	N ₁₅
charge	−0.768	−0.709	−0.788	−0.734	−0.370	−0.301	−0.354	−0.306
Dy–O/N	2.324	2.313	2.282	2.279	2.531	2.576	2.567	2.562
θ	38.1	20.5						
ESP(ax)	0.593							
Compound 4-Dy2								
	O ₄ -a	O ₆ -a	O ₃	O ₅	O ₇	O ₈	N ₁₁	N ₁₆
charge	−0.776	−0.680	−0.781	−0.695	−0.677	−0.737	−0.179	−0.170
Dy–O/N	2.295	2.279	2.248	2.327	2.304	2.315	2.585	2.550
θ	21.0	17.8						
ESP(ax) ^b	0.598							

^a“a” indicates the two axial atoms that lie closest to the magnetic easy axis within the first sphere. ^bOnly the θ values of the two axial atoms are shown. ^cESP(ax) is the semiquantitative estimate of the axial electrostatic repulsion in atomic units (au).

3, **1** has the largest value of ESP(ax), suggesting that the ESP from the axial atoms of **1** is the strongest among all of the systems here. Thus, our semiquantitative analysis does support that **1** has the best SMM properties because of its best fulfillment of the electrostatic route. In comparison, the ESP(ax) values of the mononuclear fragments of dinuclear **2** (~0.63 au) and **4** (~0.60 au) are clearly smaller than those of mononuclear **1** (0.75 au) and **3** (0.74 au). These results are also consistent with the theoretical prediction of τ_{QTM} above.

In our previous work, two new Dy(III) compounds, [Dy(L)(Dppd)]·solvent and [Dy(L)(Dppd)]^{5b}, were obtained through the same multidentate Schiff base ligand and a similar β -diketonate ligand. The two compounds also exhibit mononuclear structures, belonging to an approximate trigonal dodecahedron (D_{2d}) configuration. However, different average distances of the Dy(III)–O and Dy(III)–N bond lengths are observed. Magnetic studies reveal that these compounds display slow magnetic relaxation behavior under a 0 Oe dc field with U_{eff} of 221.38, 278.56, 247.3, and 78.0 K for

[Dy(L)(Dppd)]·solvent, [Dy(L)(Dppd)], **1**, and **3**, respectively. On the basis of theoretical analysis, the calculated ground-state g_Z values are 19.837 ($g_{XY} = 0.003$), 19.841 ($g_{XY} = 0.001$), 19.9067 ($g_{XY} = 0.002$), and 19.9023 ($g_{XY} = 0.004$) for [Dy(L)(Dppd)]·solvent, [Dy(L)(Dppd)], **1**, and **3**, respectively. The g_Z values are very similar. The g_X and g_Y values are slightly different, corresponding to the different zero-field SMM properties. The large g_{XY} value could cause more obvious QTM (eq 1d). Obviously, [Dy(L)(Dppd)] would present a more significant axial anisotropy compared to [Dy(L)(Dppd)]·solvent, **1**, and **3** based on the g_{XY} values. Experimentally, [Dy(L)(Dppd)] exhibits the highest U_{eff} value.

[Dy(L)(Dppd)]₃·solvent,^{5b} **2**, and **4** show dinuclear cores in which the metal centers are bridged by two phenol O atoms of one L²⁻ ligand or one H₂Lox²⁻ ligand. The Dy(III)···Dy(III) distances are 3.9031, 3.8840, and 3.8223(12) Å in [Dy(L)(Dppd)]₂·solvent, **2**, and **4**, respectively. The Dy(III)–O–Dy(III) angles of [Dy(L)(Dppd)]₂·solvent are 113.2(3) and 115.8(3)°. The Dy(III)–O–Dy(III) angles of **2** are 113.5(4)

and 115.9(4)°. The Dy(III)–O–Dy(III) angles of **4** are 113.5(3) and 113.2(4)°. The minimum distances and average bond angles can be observed in compound **4**. [Dy(L)(Dppd)₂]*·*solvent and **2** show similar Dy(III)–O–Dy(III) angles and Dy(III)⋯Dy(III) distances. These different distances and angles would provide different magnetic coupling pathways between Dy(III) ions.^{58–60} The Dy(III)⋯Dy(III) interactions in [Dy(L)(Dppd)₂]*·*solvent, **2**, and **4** are very weak FM. The dipolar parameters J_{dip} are calculated to be 1.66 cm⁻¹ in [Dy(L)(Dppd)₂]*·*solvent, 3.02 cm⁻¹ in **2**, and 2.56 cm⁻¹ in **4**, which are consistent with the experimental results of weak FM coupling in them. The J_{dip} value in **2** is stronger than those of [Dy(L)(Dppd)₂]*·*solvent and **4**. However, the calculated orientations of the local main magnetic axes on the Dy(III) ions in the ground-state KDs of [Dy(L)(Dppd)₂]*·*solvent exhibit a smaller angle (56.1°) than those of compounds **2** (112.3°) and **4** (128.8°) (Figure 15). Obviously, the easy axes of **2** and **4** are not parallel to the vector connecting the Dy(III) ions. This deviation would lead to transversal components of the dipolar field, which significantly increase the efficiency of the tunneling mechanism.^{59,61} Additionally, the calculated ground-state g_z values are 18.933 ($g_x, g_y = 0.147, 0.346$) and 19.286 ($g_x, g_y = 0.010, 0.014$) for [Dy(L)(Dppd)₂]*·*solvent, 18.278 ($g_x, g_y = 0.145, 0.349$) and 18.677 ($g_x, g_y = 0.242, 0.741$) for **2**, and 18.122 ($g_x, g_y = 0.338, 0.102$) and 19.103 ($g_x, g_y = 0.209, 0.420$) for **4**, respectively. Obviously, the high values of g_x and g_y in **2** and **4** would lead to strong QTM. Finally, [Dy(L)(Dppd)₂]*·*solvent displays SMM behavior under a 0 Oe dc field with U_{eff} of 162.92 K. The unparallel easy axis and high values of g_x and g_y are responsible for field-induced SMM behavior in **2** and **4**. It is well-known that the Dy(III)–O–Dy(III) angles have a significant impact on the magnetic exchange. The overlap between the magnetic orbitals of the Dy(III) ions would be modified through the Dy(III)–O–Dy(III) angles.^{61–64} For compound [Dy₂ovph₂Cl₂(MeOH)₃]*·*MeCN (H₂ovph = pyridine-2-carboxylic acid [(2-hydroxy-3-methoxyphenyl)methylene]hydrazide),⁶⁴ the two eight-coordinated metal ions are linked through the alkoxido groups (O1 and O4) of two antiparallel, or “head-to-tail”, ovph²⁻ ligands to generate a binuclear unit. The Dy(III)⋯Dy(III) distance is 3.8644(5) Å. The two Dy(III)–O–Dy(III) angles are 112.3(2) and 111.5(2)°. The corresponding local anisotropy axes of the two Dy(III) ions are almost parallel to each other. The compound presents stronger intramolecular ferromagnetic interactions. Meanwhile, excellent SMM behavior can be observed in [Dy₂ovph₂Cl₂(MeOH)₃]*·*MeCN. Additionally, ab initio calculations of magnetic interactions and magnetic axis inclination in [Dy₂(L)(NO₃)₃(CH₃O)] and [Dy₂(L)(NO₃)₃(CH₃CH₂O)] reveal the significance of the Dy(III)–O–Dy(III) angles and the direction of the easy axis. The two important criteria above would regulate f–f interactions and further impact the magnetic performances of binuclear SMMs.^{65–68}

CONCLUSIONS

In situ ligand formation was exhibited in the synthetic processes from mononuclear to binuclear Dy(III) compounds. The crystals of **1** and **3** underwent dissolution/precipitation processes and changed into **2** and **4**, respectively. The formylbenzyl groups of H₂L in **1** and **3** were changed to the (hydroxyiminomethyl)benzyl groups of H₄Lox in **2** and **4**, respectively. Compounds **1** and **3** exhibit mononuclear

structures, while compounds **2** and **4** are binuclear cores. The metal centers in **2** or **4** are bridged by two phenol O⁻ atoms of one H₂Lox²⁻ ligand. **1** and **3** show slow magnetic relaxation behavior under a 0 Oe dc field with U_{eff} of 247.3 and 78.0 K, respectively. The obvious butterfly-shaped hysteresis loops can be observed from 2 to 5 K in **1**. However, **3** shows weak butterfly-shaped hysteresis loop at 2 K. Interestingly, two relaxation processes are presented under a 1200 or 1500 Oe dc field, corresponding to the FR and SR phases in **2**, respectively. The FR process in compound **2** may result from QTM. It can be enhanced by dipolar interactions between the Dy(III) ions or the presence of an applied field. A similar phenomenon can be seen in **4**. The KD₀ of **1** is of a high degree of axiality, which leads to weak QTM. Additionally, theoretical τ_{QTM} values are also consistent with the experimental values in that τ_{QTM} of **1** is longer than those of **2–4**. In other words, QTM of **1** is weaker than that of **2–4**. This is consistent with the experimental observations of apparent SMM behavior in **1** under a 0 Oe dc field, while **2–4** show weak slow magnetic relaxation behavior. According to the results of the constituent mononuclear Dy(III) fragments, the dipolar parameters J_{dip} in **2** and **4** were calculated to be 3.02 and 2.56 cm⁻¹, respectively. They are consistent with the experimental results of weak FM coupling. This work presents an efficient approach to designing and synthesizing Ln compounds with different structures for in situ Schiff base reaction and provides a new method for magnetic regulation.

ASSOCIATED CONTENT

Supporting Information

The Supporting Information is available free of charge at <https://pubs.acs.org/doi/10.1021/acs.inorgchem.0c02863>.

Structural and magnetic characterization and theoretical calculation (PDF)

Accession Codes

CCDC 1947756, 1947757, 2024916, and 2024917 contain the supplementary crystallographic data for this paper. These data can be obtained free of charge via www.ccdc.cam.ac.uk/data_request/cif, or by emailing data_request@ccdc.cam.ac.uk, or by contacting The Cambridge Crystallographic Data Centre, 12 Union Road, Cambridge CB2 1EZ, UK; fax: +44 1223 336033.

AUTHOR INFORMATION

Corresponding Authors

Sheng Zhang – Faculty of Chemistry and Chemical Engineering, Engineering Research Center of Advanced Ferroelectric Functional Materials, Key Laboratory of Phytochemistry of Shaanxi Province, Baoji University of Arts and Sciences, Baoji, Shaanxi 721013, China; orcid.org/0000-0001-9370-0548; Email: zhangsheng19890501@163.com

Sanping Chen – Key Laboratory of Synthetic and Natural Functional Molecule of the Ministry of Education, College of Chemistry and Materials Science, Northwest University, Xi'an, Shaanxi 710127, China; orcid.org/0000-0002-6851-7386; Email: sanpingchen@126.com

Bing Yin – Key Laboratory of Synthetic and Natural Functional Molecule of the Ministry of Education, College of Chemistry and Materials Science, Northwest University, Xi'an, Shaanxi 710127, China; orcid.org/0000-0001-8668-9504; Email: rayinyin@nwu.edu.cn

Jiangwei Zhang – Dalian National Laboratory for Clean Energy and State Key Laboratory of Catalysis, Dalian Institute of Chemical Physics, Chinese Academy of Sciences, Dalian 116023, P. R. China; orcid.org/0000-0002-1221-3033; Email: jwzhang@dicp.ac.cn

Authors

Jiamin Tang – Faculty of Chemistry and Chemical Engineering, Engineering Research Center of Advanced Ferroelectric Functional Materials, Key Laboratory of Phytochemistry of Shaanxi Province, Baoji University of Arts and Sciences, Baoji, Shaanxi 721013, China

Jin Zhang – Faculty of Chemistry and Chemical Engineering, Engineering Research Center of Advanced Ferroelectric Functional Materials, Key Laboratory of Phytochemistry of Shaanxi Province, Baoji University of Arts and Sciences, Baoji, Shaanxi 721013, China

Fang Xu – Faculty of Chemistry and Chemical Engineering, Engineering Research Center of Advanced Ferroelectric Functional Materials, Key Laboratory of Phytochemistry of Shaanxi Province, Baoji University of Arts and Sciences, Baoji, Shaanxi 721013, China

Dengwei Hu – Faculty of Chemistry and Chemical Engineering, Engineering Research Center of Advanced Ferroelectric Functional Materials, Key Laboratory of Phytochemistry of Shaanxi Province, Baoji University of Arts and Sciences, Baoji, Shaanxi 721013, China; orcid.org/0000-0001-7961-7115

Complete contact information is available at: <https://pubs.acs.org/10.1021/acs.inorgchem.0c02863>

Author Contributions

The manuscript was written through contributions of all authors. All authors have given approval to the final version of the manuscript. B.Y. is responsible for the theoretical part of this work including ab initio calculation and theoretical interpretation of magnetic anisotropy and dynamics.

Notes

The authors declare no competing financial interest.

ACKNOWLEDGMENTS

We gratefully acknowledge financial support from the National Natural Science Foundation of China (Grants 21703002, 21727805, and 21673180), the Young Talent Fund of University Association for Science and Technology in Shaanxi, China (Grant 20200610), the Special Scientific Research Project of Education Department of Shaanxi Provincial Government (Grant 20JK0484), the Natural Science Basic Research Plan in Shaanxi Province of China (Grant 2019JQ-180), the Open Foundation of Key Laboratory of Synthetic and Natural Functional Molecule Chemistry of Ministry of Education [Grant 338050067(2018-008)], the National Undergraduate Training Programs for Innovation and Entrepreneurship (Grant S202010721006), and the Doctoral Scientific Research Starting Foundation of Baoji University of Arts and Science (Grant ZK2017024).

REFERENCES

(1) (a) Gatteschi, D.; Sessoli, R.; Villain, J. *Molecular nanomagnets*; Oxford University Press: Oxford, U.K., 2006. (b) Mannini, M.; Pineider, F.; Danieli, C.; Totti, F.; Sorace, L.; Sainctavit, P.; Arrio, M. A.; Otero, E.; Joly, L.; Cezar, J. C.; Cornia, A.; Sessoli, R. Quantum

tunnelling of the magnetization in a monolayer of oriented single-molecule magnets. *Nature* **2010**, *468*, 417.

(2) Habib, F.; Murugesu, M. Lessons learned from dinuclear lanthanide nano-magnets. *Chem. Soc. Rev.* **2013**, *42*, 3278–3288.

(3) Ishikawa, N.; Sugita, M.; Ishikawa, T.; Koshihara, S. y.; Kaizu, Y. Lanthanide double-decker complexes functioning as magnets at the single molecular level. *J. Am. Chem. Soc.* **2003**, *125*, 8694–8695.

(4) Zhang, P.; Guo, Y. N.; Tang, J. K. Recent advances in dysprosium-based single molecule magnets: Structural overview and synthetic strategies. *Coord. Chem. Rev.* **2013**, *257*, 1728–1763.

(5) (a) Li, X. L.; Tang, J. K. Recent developments in single-molecule toroids. *Dalton Trans.* **2019**, *48*, 15358–15370. (b) Zhang, S.; Mo, W. J.; Zhang, Z. Q.; Gao, F.; Wang, L.; Hu, D. W.; Chen, S. P. Ligand ratio/solvent-influenced syntheses, crystal structures, and magnetic properties of polydentate Schiff base ligand-Dy (III) compounds with β -diketonate ligands as co-ligands. *Dalton Trans.* **2019**, *48*, 12466–12481. (c) Zhu, Z. H.; Li, X. L.; Liu, S. T.; Tang, J. K. External stimuli modulate the magnetic relaxation of lanthanide single-molecule magnets. *Inorg. Chem. Front.* **2020**, *7*, 3315–3326. (d) Wu, J. F.; Cador, O.; Li, X. L.; Zhao, L.; Le Guennic, B.; Tang, J. K. Axial ligand field in D_{4d} coordination symmetry: magnetic relaxation of Dy SMMs perturbed by counteranions. *Inorg. Chem.* **2017**, *56*, 11211–11219.

(e) Wang, W. M.; Wang, S. Y.; Zhang, H. X.; Shen, H. Y.; Zou, J. Y.; Gao, H. L.; Cui, J. Z.; Zhao, B. Modulating single-molecule magnet behaviour of phenoxo-O bridged lanthanide (iii) dinuclear complexes by using different β -diketonate coligands. *Inorg. Chem. Front.* **2016**, *3*, 133–141. (f) Bala, S.; Bishwas, M. S.; Pramanik, B.; Khanra, S.; Fromm, K. M.; Poddar, P.; Mondal, R. Construction of polynuclear lanthanide ($\text{Ln} = \text{Dy}^{\text{III}}$, Tb^{III} and Nd^{III}) cage complexes using pyridine–pyrazole-based ligands: versatile molecular topologies and SMM behavior. *Inorg. Chem.* **2015**, *54*, 8197–8206. (g) Wang, W. M.; Kang, X. M.; Shen, H. Y.; Wu, Z. L.; Gao, H. L.; Cui, J. Z. Modulating single-molecule magnet behavior towards multiple magnetic relaxation processes through structural variation in Dy_4 clusters. *Inorg. Chem. Front.* **2018**, *5*, 1876–1885. (h) Wang, W. M.; Wu, Z. L.; Zhang, Y. X.; Wei, H. Y.; Gao, H. L.; Cui, J. Z. Self-assembly of tetranuclear lanthanide clusters via atmospheric CO_2 fixation: interesting solvent-induced structures and magnetic relaxation conversions. *Inorg. Chem. Front.* **2018**, *5*, 2346–2354. (i) Wang, W. M.; He, L. Y.; Wang, X. X.; Shi, Y.; Wu, Z. L.; Cui, J. Z. Linear-shaped Ln^{III}_4 and Ln^{III}_6 clusters constructed by a polydentate Schiff base ligand and a β -diketonate co-ligand: structures, fluorescence properties, magnetic refrigeration and single-molecule magnet behavior. *Dalton Trans.* **2019**, *48*, 16744–16755.

(6) Liu, K.; Zhang, X.; Meng, X.; Shi, W.; Cheng, P.; Powell, A. K. Constraining the coordination geometries of lanthanide centers and magnetic building blocks in frameworks: a new strategy for molecular nanomagnets. *Chem. Soc. Rev.* **2016**, *45*, 2423–2439.

(7) Meng, Y. S.; Jiang, S. D.; Wang, B. W.; Gao, S. Understanding the magnetic anisotropy toward single-ion magnets. *Acc. Chem. Res.* **2016**, *49*, 2381–2389.

(8) Pointillart, F.; Cador, O.; Le Guennic, B.; Ouahab, L. Uncommon lanthanide ions in purely 4f single molecule magnets. *Coord. Chem. Rev.* **2017**, *346*, 150–175.

(9) Liu, J. L.; Chen, Y. C.; Tong, M. L. Symmetry strategies for high performance lanthanide-based single-molecule magnets. *Chem. Soc. Rev.* **2018**, *47*, 2431–2453.

(10) Zhu, Z. H.; Guo, M.; Li, X. L.; Tang, J. K. Molecular magnetism of lanthanide: Advances and perspectives. *Coord. Chem. Rev.* **2019**, *378*, 350–364.

(11) Yutronkie, N. J.; Kühne, I. A.; Korobkov, I.; Brusso, J. L.; Murugesu, M. Connecting mononuclear dysprosium single-molecule magnets to form dinuclear complexes via in situ ligand oxidation. *Chem. Commun.* **2016**, *52*, 677–680.

(12) Chesman, A. S. R.; Turner, D. R.; Moubaraki, B.; Murray, K. S.; Deacon, G. B.; Batten, S. R. In situ ligand formation in the synthesis of an octanuclear dysprosium ‘double cubane’ cluster displaying single molecule magnet features. *Dalton Trans.* **2012**, *41*, 3751–3757.

- (13) Liang, L.; Peng, G.; Li, G.; Lan, Y.; Powell, A. K.; Deng, H. In situ hydrothermal synthesis of dysprosium (III) single-molecule magnet with lanthanide salt as catalyst. *Dalton Trans.* **2012**, *41*, 5816–5823.
- (14) Firmo, R. N.; de Souza, I. C. A.; da Silva Miranda, F.; Pinheiro, C. B.; Resende, J. A. L. C.; Lanznaster, M. A new ligand H_4Lox and its iron(III) complex as a platform for the development of hetero-trimetallic complexes. *Polyhedron* **2016**, *117*, 604–611.
- (15) Zhang, H. X.; Lin, S. Y.; Xue, S. F.; Wang, C.; Tang, J. K. Acetato-bridged dinuclear lanthanide complexes with single molecule magnet behaviour for the Dy_2 species. *Dalton Trans.* **2014**, *43*, 6262–6268.
- (16) Liu, J.; Chen, Y. C.; Liu, J. L.; Vieru, V.; Ungur, L.; Jia, J. H.; Chibotaru, L. F.; Lan, Y. H.; Wernsdorfer, W.; Gao, S.; Chen, X. M.; Tong, M. L. A stable pentagonal bipyramidal $Dy(III)$ single-ion magnet with a record magnetization reversal barrier over 1000 K. *J. Am. Chem. Soc.* **2016**, *138*, 5441–5450.
- (17) Ruiz, J.; Mota, A. J.; Rodríguez-Díéguez, A.; Titos, S.; Herrera, J. M.; Ruiz, E.; Cremades, E.; Costes, J. P.; Colacio, E. Field and dilution effects on the slow relaxation of a luminescent DyO_9 low-symmetry single-ion magnet. *Chem. Commun.* **2012**, *48*, 7916–7918.
- (18) Jiang, Z. J.; Sun, L.; Yang, Q.; Yin, B.; Ke, H. S.; Han, J.; Wei, Q.; Xie, G.; Chen, S. P. Excess axial electrostatic repulsion as a criterion for pentagonal bipyramidal Dy^{III} single-ion magnets with high U_{eff} and T_B . *J. Mater. Chem. C* **2018**, *6*, 4273–4280.
- (19) Sheldrick, G. M. *SADABS, Program for empirical absorption correction*; University of Göttingen: Göttingen, Germany, 1996.
- (20) (a) Sheldrick, G. M. SHELXT-Integrated space-group and crystal-structure determination. *Acta Crystallogr., Sect. A: Found. Adv.* **2015**, *A71*, 3–8. (b) Sheldrick, G. M. A short history of SHELX. *Acta Crystallogr., Sect. A: Found. Crystallogr.* **2008**, *A64*, 112–122.
- (21) Llundell, M.; Casanova, D.; Cirera, J.; Alemany, P.; Alvarez, S. *SHAPE*, version 2.1; University of Barcelona: Barcelona, Spain, 2013.
- (22) Casanova, D.; Llundell, M.; Alemany, P.; Alvarez, S. The rich stereochemistry of eight-vertex polyhedra: a continuous shape measures study. *Chem. - Eur. J.* **2005**, *11*, 1479–1494.
- (23) (a) Tang, J. K.; Hewitt, I.; Madhu, N. T.; Chastanet, G.; Wernsdorfer, W.; Anson, C. E.; Benelli, C.; Sessoli, R.; Powell, A. K. Dysprosium triangles showing single-molecule magnet behavior of thermally excited spin states. *Angew. Chem., Int. Ed.* **2006**, *45*, 1729–1733. (b) Guo, Y. N.; Xu, G. F.; Gamez, P.; Zhao, L.; Lin, S. Y.; Deng, R.; Tang, J. K.; Zhang, H. J. Two-step relaxation in a linear tetranuclear dysprosium (III) aggregate showing single-molecule magnet behavior. *J. Am. Chem. Soc.* **2010**, *132*, 8538–8539. (c) Zhang, S.; Mo, W. J.; Yin, B.; Zhang, G. N.; Yang, D.-S.; Lü, X. Q.; Chen, S. P. The slow magnetic relaxation regulated by the coordination, configuration and intermolecular dipolar field in two mononuclear Dy^{III} single-molecule magnets (SMMs). *Dalton Trans.* **2018**, *47*, 12393–12405. (d) Liu, X. Y.; Ma, X. F.; Yuan, W. Z.; Cen, P. P.; Zhang, Y. Q.; Ferrando-Soria, J.; Xie, G.; Chen, S. P.; Pardo, E. Concise chemistry modulation of the SMM behavior within a family of mononuclear $Dy(III)$ complexes. *Inorg. Chem.* **2018**, *57*, 14843–14851. (e) Zhang, S.; Mo, W. J.; Zhang, J. W.; Zhang, Z. Q.; Yin, B.; Hu, D. W.; Chen, S. P. Regulation of substituent effects on configurations and magnetic performances of mononuclear Dy^{III} single-molecule magnets. *Inorg. Chem.* **2019**, *58*, 15330–15343. (f) Zhang, S.; Ke, H. S.; Liu, X. Y.; Wei, Q.; Xie, G.; Chen, S. P. A nine-coordinated dysprosium (III) compound with an oxalate-bridged dysprosium (III) layer exhibiting two slow magnetic relaxation processes. *Chem. Commun.* **2015**, *51*, 15188–15191. (g) Bernot, K.; Luzon, J.; Bogani, L.; Etienne, M.; Sangregorio, C.; Shanmugam, M.; Caneschi, A.; Sessoli, R.; Gatteschi, D. Magnetic anisotropy of dysprosium (III) in a low-symmetry environment: A theoretical and experimental investigation. *J. Am. Chem. Soc.* **2009**, *131*, 5573–5579. (h) Xi, L.; Li, H. D.; Sun, J.; Ma, Y.; Tang, J. K.; Li, L. C. Designing multicoordinating nitronyl nitroxide radical toward multinuclear lanthanide aggregates. *Inorg. Chem.* **2020**, *59*, 443–451.
- (24) Luzon, J.; Sessoli, R. Lanthanides in molecular magnetism: so fascinating, so challenging. *Dalton Trans.* **2012**, *41*, 13556–13567.
- (25) Roos, B. O.; Taylor, P. R.; Siegbahn, P. E. M. A complete active space SCF method (CASSCF) using a density matrix formulated super-CI approach. *Chem. Phys.* **1980**, *48*, 157–173.
- (26) Malmqvist, P.; Roos, B. O.; Schimmelpfennig, B. The restricted active space (RAS) state interaction approach with spin-orbit coupling. *Chem. Phys. Lett.* **2002**, *357*, 230–240.
- (27) Hess, B. A.; Marian, C. M.; Wahlgren, U.; Gropen, O. A mean-field spin-orbit method applicable to correlated wavefunctions. *Chem. Phys. Lett.* **1996**, *251*, 365–371.
- (28) Roos, B. O.; Lindh, R.; Malmqvist, P.; Veryazov, V.; Widmark, P. Main group atoms and dimers studied with a new relativistic ANO basis set. *J. Phys. Chem. A* **2004**, *108*, 2851–2858.
- (29) Roos, B. O.; Lindh, R.; Malmqvist, P.; Veryazov, V.; Widmark, P. New relativistic ANO basis sets for transition metal atoms. *J. Phys. Chem. A* **2005**, *109*, 6575–6579.
- (30) Roos, B. O.; Lindh, R.; Malmqvist, P.; Veryazov, V.; Widmark, P.; Borin, A. C. New relativistic atomic natural orbital basis sets for lanthanide atoms with applications to the Ce diatom and LuF_3 . *J. Phys. Chem. A* **2008**, *112*, 11431–11435.
- (31) Chibotaru, L. F.; Ungur, L. Ab initio calculation of anisotropic magnetic properties of complexes. I. Unique definition of pseudospin Hamiltonians and their derivation. *J. Chem. Phys.* **2012**, *137*, 064112.
- (32) Chibotaru, L. F. Ab initio methodology for pseudospin Hamiltonians of anisotropic magnetic complexes. *Adv. Chem. Phys.* **2013**, *153*, 397–519.
- (33) Aquilante, F.; De Vico, L.; Ferre, N.; Ghigo, G.; Malmqvist, P. A.; Neogrady, P.; Pedersen, T. B.; Pitonak, M.; Reiher, M.; Roos, B. O.; Serrano-Andres, L.; Urban, M.; Veryazov, V.; Lindh, R. Molcas 7: The next generation. *J. Comput. Chem.* **2010**, *31*, 224–247.
- (34) Aquilante, F.; Autschbach, J.; Carlson, R. K.; Chibotaru, L. F.; Delcey, M. G.; De Vico, L.; Fdez. Galvan, I.; Ferre, N.; Frutos, L. M.; Gagliardi, L.; Garavelli, M.; Giussani, A.; Hoyer, C. E.; Li Manni, G.; Lischka, H.; Ma, D.; Malmqvist, P. A.; Muller, T.; Nenov, A.; Olivucci, M.; Pedersen, T. B.; Peng, D.; Plasser, F.; Pritchard, B.; Reiher, M.; Rivalta, I.; Schapiro, I.; Segarra-Marti, J.; Stenrup, M.; Truhlar, D. G.; Ungur, L.; Valentini, A.; Vancoillie, S.; Veryazov, V.; Vysotskiy, V. P.; Weingart, O.; Zapata, F.; Lindh, R. Molcas 8: New capabilities for multiconfigurational quantum chemical calculations across the periodic table. *J. Comput. Chem.* **2016**, *37*, 506–541.
- (35) Chibotaru, L. F. Theoretical understanding of anisotropy in molecular nanomagnets. *Struct. Bonding (Berlin, Ger.)* **2014**, *164*, 185–230.
- (36) Alonso, P. J.; Martínez, J. I. Magnetic properties of a Kramers doublet. An univocal bridge between experimental results and theoretical predictions. *J. Magn. Reson.* **2015**, *255*, 1–14.
- (37) Liddle, S. T.; van Slageren, J. Improving f-element single molecule magnets. *Chem. Soc. Rev.* **2015**, *44*, 6655–6669.
- (38) Ungur, L.; Chibotaru, L. F. Strategies toward high-temperature lanthanide-based single-molecule magnets. *Inorg. Chem.* **2016**, *55*, 10043–10056.
- (39) Li, M.; Wu, H. P.; Yang, Q.; Ke, H. S.; Yin, B.; Shi, Q.; Wang, W. Y.; Wei, Q.; Xie, G.; Chen, S. P. Experimental and theoretical interpretation on the magnetic behavior in a series of pentagonal-bipyramidal Dy^{III} single-ion magnets. *Chem. - Eur. J.* **2017**, *23*, 17775–17787.
- (40) Ungur, L.; Chibotaru, L. F. Magnetic anisotropy in the excited states of low symmetry lanthanide complexes. *Phys. Chem. Chem. Phys.* **2011**, *13*, 20086–20090.
- (41) Ungur, L.; Chibotaru, L. F. Lanthanides and actinides in molecular magnetism. In *Computational modelling of the magnetic properties of lanthanide compounds*, 1st ed.; Layfield, R. A., Murugesu, M., Eds.; Wiley-VCH Verlag GmbH & Co. KGaA, 2015; Chapter 6, pp 153–184.
- (42) Bartolomé, E.; Arauzo, A.; Luzón, J.; Bartolomé, J.; Bartolomé, F. Magnetic relaxation of lanthanide-based molecular magnets. *Handbook of Magnetic Materials*; Elsevier BV, 2017; Vol. 26, Chapter 1.

- (43) Gatteschi, D.; Sessoli, R.; Villain, J. Spin–phonon interaction. *Molecular Nanomagnets*; Oxford University Press: Oxford, U.K., 2006; Chapter 5.5, pp 167–171.
- (44) Gatteschi, D.; Sessoli, R. Quantum tunneling of magnetization and related phenomena in molecular materials. *Angew. Chem., Int. Ed.* **2003**, *42*, 268–297.
- (45) Yin, B.; Li, C.-C. A method to predict both the relaxation time of quantum tunneling of magnetization and the effective barrier of magnetic reversal for a Kramers single-ion magnet. *Phys. Chem. Chem. Phys.* **2020**, *22*, 9923–9933.
- (46) Aravena, D. Ab initio prediction of tunneling relaxation times and effective demagnetization barriers in kramers lanthanide single-molecule magnets. *J. Phys. Chem. Lett.* **2018**, *9*, 5327–5333.
- (47) Zhu, Z. H.; Wang, H. F.; Yu, S.; Zou, H.-H.; Wang, H. L.; Yin, B.; Liang, F. P. Substitution effects regulate the formation of butterfly-shaped tetranuclear Dy (III) cluster and Dy-based hydrogen-bonded helix frameworks: structure and magnetic properties. *Inorg. Chem.* **2020**, *59*, 11640–11650.
- (48) Gatteschi, D.; Sessoli, R.; Villain, J. *Molecular Nanomagnets*; Oxford University Press: Oxford, U.K., 2006; pp 161–163.
- (49) Woodruff, D. N.; Winpenny, R. E. P.; Layfield, R. A. Lanthanide single-molecule magnets. *Chem. Rev.* **2013**, *113*, 5110–5148.
- (50) Gatteschi, D.; Sessoli, R.; Villain, J. Relaxation and relaxation time. *Molecular Nanomagnets*; Oxford University Press: Oxford, U.K., 2006; Chapter 5.1, pp 160–161.
- (51) Aravena, D.; Ruiz, E. Shedding light on the single-molecule magnet behavior of mononuclear Dy^{III} complexes. *Inorg. Chem.* **2013**, *52*, 13770–13778.
- (52) Zhang, S.; Wu, H. P.; Sun, L.; Ke, H. S.; Chen, S. P.; Yin, B.; Wei, Q.; Yang, D. S.; Gao, S. L. Ligand field fine-tuning on the modulation of the magnetic properties and relaxation dynamics of dysprosium (III) single-ion magnets (SIMs): synthesis, structure, magnetism and ab initio calculations. *J. Mater. Chem. C* **2017**, *5*, 1369–1382.
- (53) Jiang, Z. J.; Sun, L.; Yang, Q.; Yin, B.; Ke, H. S.; Han, J.; Wei, Q.; Xie, G.; Chen, S. P. Excess axial electrostatic repulsion as a criterion for pentagonal bipyramidal Dy^{III} single-ion magnets with high U_{eff} and T_{B} . *J. Mater. Chem. C* **2018**, *6*, 4273–4280.
- (54) Guo, M.; Wu, J. F.; Cador, O.; Lu, J. J.; Yin, B.; Le Guennic, B.; Tang, J. K. Manipulating the relaxation of quasi- D_{4d} dysprosium compounds through alternation of the O-donor ligands. *Inorg. Chem.* **2018**, *57*, 4534–4542.
- (55) Sievers, Z. A sphericity of 4f-shells in their Hund's rule ground states. *Z. Phys. B: Condens. Matter Quanta* **1982**, *45*, 289–296.
- (56) Rinehart, J. D.; Long, J. R. Exploiting single-ion anisotropy in the design of f-element single-molecule magnets. *Chem. Sci.* **2011**, *2*, 2078–2085.
- (57) Ungur, L.; Chibotaru, L. F. Ab initio crystal field for lanthanides. *Chem. - Eur. J.* **2017**, *23*, 3708–3718.
- (58) Tu, H. R.; Sun, W. B.; Li, H. F.; Chen, P.; Tian, Y. M.; Zhang, W. Y.; Zhang, Y. Q.; Yan, P. F. Complementation and joint contribution of appropriate intramolecular coupling and local ion symmetry to improve magnetic relaxation in a series of dinuclear Dy₂ single-molecule magnets. *Inorg. Chem. Front.* **2017**, *4*, 499–508.
- (59) Sun, L.; Wei, S. L.; Zhang, J.; Wang, W. Y.; Chen, S. P.; Zhang, Y. Q.; Wei, Q.; Xie, G.; Gao, S. L. Isomeric ligands enhance the anisotropy barrier within nine-coordinated {Dy₂} compounds. *J. Mater. Chem. C* **2017**, *5*, 9488–9495.
- (60) Yang, Z. F.; Tian, Y. M.; Zhang, W. Y.; Chen, P.; Li, H. F.; Zhang, Y. Q.; Sun, W. B. High local coordination symmetry around the spin center and the alignment between magnetic and symmetric axes together play a crucial role in single-molecule magnet performance. *Dalton Trans.* **2019**, *48*, 4931–4940.
- (61) Guo, Y. N.; Xu, G. F.; Wernsdorfer, W.; Ungur, L.; Guo, Y.; Tang, J. K.; Zhang, H. J.; Chibotaru, L. F.; Powell, A. K. Strong axiality and Ising exchange interaction suppress zero-field tunneling of magnetization of an asymmetric Dy₂ single-molecule magnet. *J. Am. Chem. Soc.* **2011**, *133*, 11948–11951.
- (62) Guo, Y. N.; Chen, X. H.; Xue, S. F.; Tang, J. K. Modulating magnetic dynamics of three Dy₂ complexes through keto–enol tautomerism of the o-vanillin picolinoylhydrazone ligand. *Inorg. Chem.* **2011**, *50*, 9705–9713.
- (63) Ke, H. S.; Zhang, S.; Li, X.; Wei, Q.; Xie, G.; Wang, W. Y.; Chen, S. P. A Dy₂ single-molecule magnet with benzoate anions and phenol-O[−] bridging groups. *Dalton Trans.* **2015**, *44*, 21025–21031.
- (64) Dong, H. M.; Li, H. Y.; Zhang, Y. Q.; Yang, E. C.; Zhao, X. J. Magnetic relaxation dynamics of a centrosymmetric Dy₂ single-molecule magnet triggered by magnetic-site dilution and external magnetic field. *Inorg. Chem.* **2017**, *56*, 5611–5622.
- (65) Zhang, S.; Shen, N.; Liu, S.; Ma, R.; Zhang, Y. Q.; Hu, D. W.; Liu, X. Y.; Zhang, J. W.; Yang, D. S. Rare CH₃O[−]/CH₃CH₂O[−]-bridged nine-coordinated binuclear Dy^{III} single-molecule magnets (SMMs) significantly regulate and enhance the effective energy barriers. *CrystEngComm* **2020**, *22*, 1712–1724.
- (66) Guo, M.; Zhang, Y. Q.; Zhu, Z. H.; Tang, J. K. Dysprosium compounds with hula-hoop-like geometries: the influence of magnetic anisotropy and magnetic interactions on magnetic relaxation. *Inorg. Chem.* **2018**, *57*, 12213–12221.
- (67) Lu, J. J.; Zhang, Y. Q.; Li, X. L.; Guo, M.; Wu, J. F.; Zhao, L.; Tang, J. K. Influence of magnetic interactions and single-ion anisotropy on magnetic relaxation within a family of tetranuclear dysprosium complexes. *Inorg. Chem.* **2019**, *58*, 5715–5724.
- (68) Jin, C. Y.; Li, X. L.; Liu, Z. L.; Mansikkamäki, A.; Tang, J. K. An investigation into the magnetic interactions in a series of Dy₂ single-molecule magnets. *Dalton Trans.* **2020**, *49*, 10477–10485.